Vertical stability of a wave powered sensor buoy

Geoffroy LESOT
EIKW95

Submitted to the
Department of Fluid Mechanics of the
Budapest University of Technology and Economics
in partial fulfillment of the requirements for the degree of
Master of Science in Mechanical Engineering Modelling

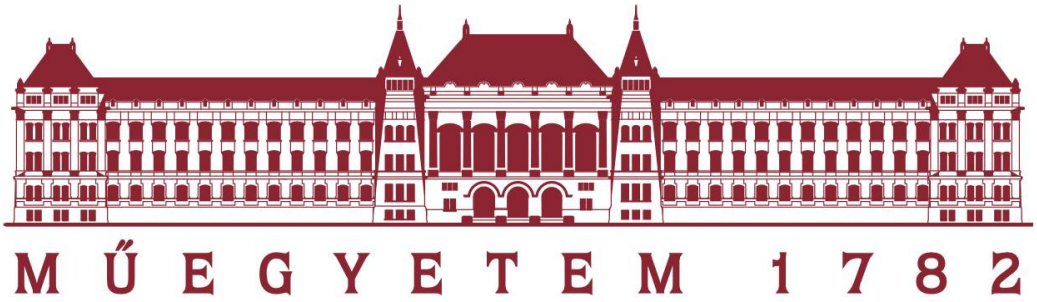

On December 13th, 2019

MSc Thesis

Final Project B /BMEGEÁTMWDB/

Supervisor and advisor:
Dr. Josh DAVIDSON, PhD

Department of Fluid Mechanics
Faculty of Mechanical Engineering
Budapest University of Technology and Economics

DECLARATION

Full Name (as in ID):	Geoffroy, Henri, Camille LESOT
Neptun Code:	EIKW95
University:	Budapest University of Technology and Economics
Faculty:	Faculty of Mechanical Engineering
Department:	Department of Fluid Mechanics
Major/Minor:	MSc in Mechanical Engineering Modelling Fluid Mechanics/Design and Technology
Thesis Title:	Vertical stability of a wave powered sensor buoy
Academic year of submission:	2019/2020 - I

I, the undersigned, hereby declare that the Thesis submitted for assessment and defence, exclusively contains the results of my own work assisted by my supervisor. Further to it, it is also stated that all other results taken from the technical literature or other sources are clearly identified and referred to according to copyright (footnotes/references are chapter and verse, and placed appropriately). I accept that the scientific results presented in my Thesis can be utilised by the Department of the supervisor for further research or teaching purposes.

Budapest, December 13th, 2019

_____

Signature

ACKNOWLEDGMENT

My thoughts naturally go to my Thesis supervisor and advisor, Dr. Josh DAVIDSON. I can't thank him enough for his dedication regarding the project, his patience and guidance that more than once kept me from getting lost in abstract notions in which I had, at first, such poor insight.

Abstract

Floating sensor buoy devices (FSBDs) are used mainly to gather data from underwater and water surface to respond to naval as well as maritime industry requests. Due to their complex access on the sea, the FSBDs are self powered. Among the renewable energy options, wave energy converters (WECs) have many advantages. One particular method to extract the consistently dense, sea wave energy, is a via heaving buoy, equipped with an internal, inertial power take-off (PTO), thereby acting as a point absorber.

A noted unresolved problem for this type of WEC, is large amplitude pitch/roll motion. This has a two-fold negative effect on the FSBD system: (1) Reduction of electrical energy from the WEC system (2) Deteriorated wireless sensor network capability, due to misalignment of vertical antenna.

Parametric resonance can be the cause of very large amplitude, unstable, pitch/roll motions in floating bodies. However, this nonlinear phenomenon, has not previously been implemented in the literature for this type of WEC-FSBD.

The objective of this study is therefore to include the effect of parametric resonance, when ensuring the vertical stability of a WEC-FSBD device.

Contents

List of Figures

1 Introduction

1.1 Marine based sensors

1.1.1 Overview

Besides playing a key role in climate regulation, oceans provide us with natural resources, recreation and a route for transport of goods and services. For these purposes, marine monitoring has lately become a field of major interest and over the past fifteen to twenty years, development of data gathering offshore buoys has been one of the top challenges of marine-linked research.
Sensor buoys seem to be a promising alternative for sea surveillance. They offer a low cost real time monitoring of the water physical and chemical parameters (see Table 1) and have various applications: water quality monitoring, ocean sensing, marine fish farm or coral reef monitoring... Some of their main advantages are their easy deployment, flexibility and energy independence. They can provide data continuously by cellular communication and Internet-based information sharing.
In practice, sensor buoys are usually deployed at sea in a large number, creating wireless sensor networks (WSNs). The SEMAT (Smart Environmental Monitoring and Analysis Technologies) have conducted researches on WSN deployment in marine environment, collecting data on climate change, water quality and ecosystem health. One of the key components of these WSNs is the data transmission system.

Table 1: Common oceanographic sensors

Measured Parameter	Unit
Temperature	$^{\circ}C$, $^{\circ}F$
Pressure	mmHg
Salinity	g/L
Water speed	m/s
Chlorophyll	μg/L
Dissolved oxygen	mg/L
Nitrate	mg/L
pH	pKa

1.1.2 Data transmission

1.1.2.1 Description of a single sensor node

A marine WSN is composed of several sensor buoys called nodes. Each node generally comprises:

- *Out-of-water part*: includes an antenna for RF transmission, surface sensors and occasionally an energy harvesting system to ensure self powering.
- *Submerged part*: composed of sensor strings, a sonde to relay data to the out-of-water part, and a mooring device to maintain the FSBD on station.
- *Internal part*: consisting of electronics, such as a CPU, a power supply regulator, an Analog/Digital converter to relay data to the antenna.

Fig.1.1 details the common features of a FSBD.

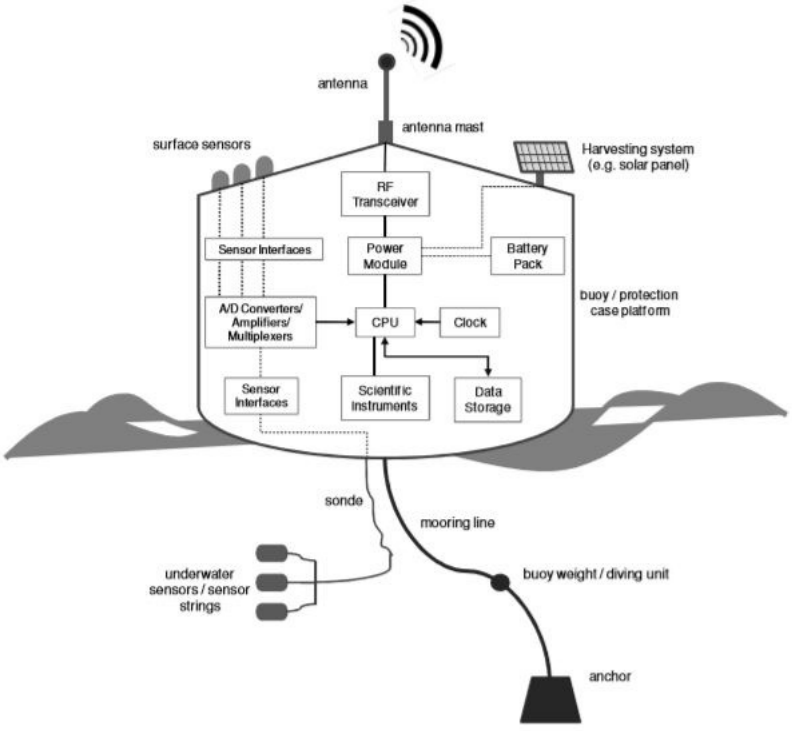

Figure 1.1: General scheme of a sensor node [1]

1.1.2.2 General architecture of a Wireless Sensor Network

Within the network, inter-node communication is handled either point-to-point (exclusive communication link between two systems) or multihop (at least 1 other station exists in the path between the source and destination). Some particular nodes, called sinks, communicate directly with the base station.

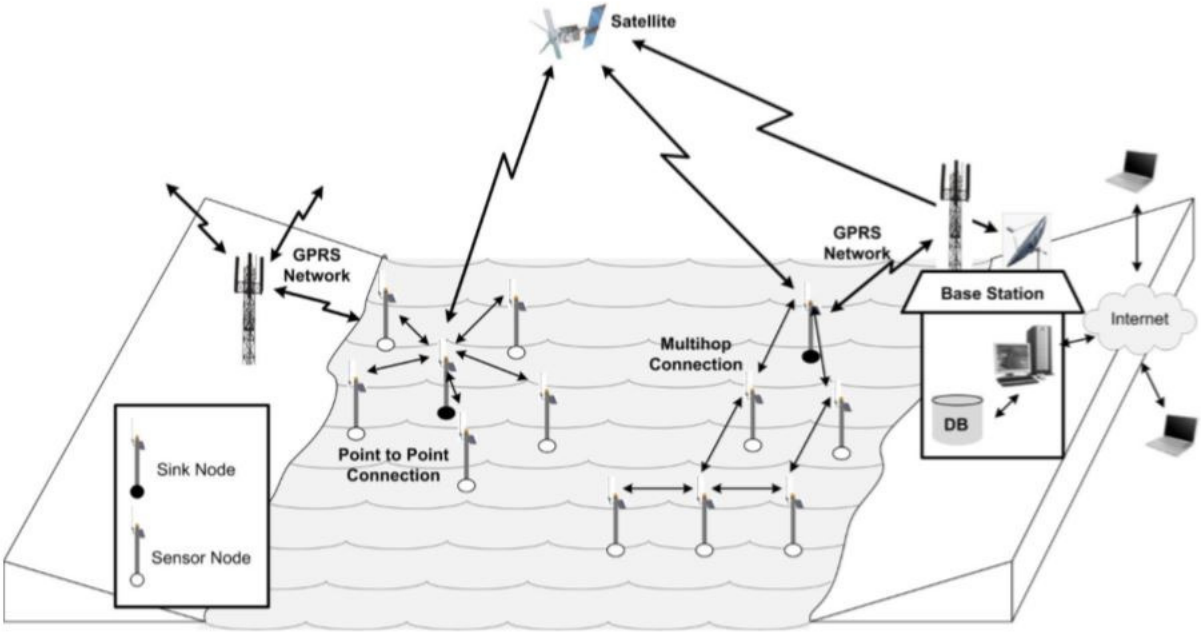

Figure 1.2: General structure of a Wireless Sensor Network [1]

1.1.3 Energy requirement

Historically, maintenance expeditions for MWSNs (Marine Wireless Sensor Networks) have demanded costly trips to remote locations, to check the functioning of the nodes, gather data and replace the batteries [8]. The "wireless" quality of a MWSN would allow us to continue integrating more sensors into our environments, but it is also the most limiting technological lock: a lack of wired connection necessarily implies energy autonomy, which is all the more problematic because wireless communication causes overconsumption of energy [2]. Several research axes are trying to solve this problem: improving manufacturing technologies and radio communication protocols to reduce node consumption, developing energy reservoirs such as batteries or fuel cells to increase their performance, or capturing ambient energy from the sensor environment to power it.

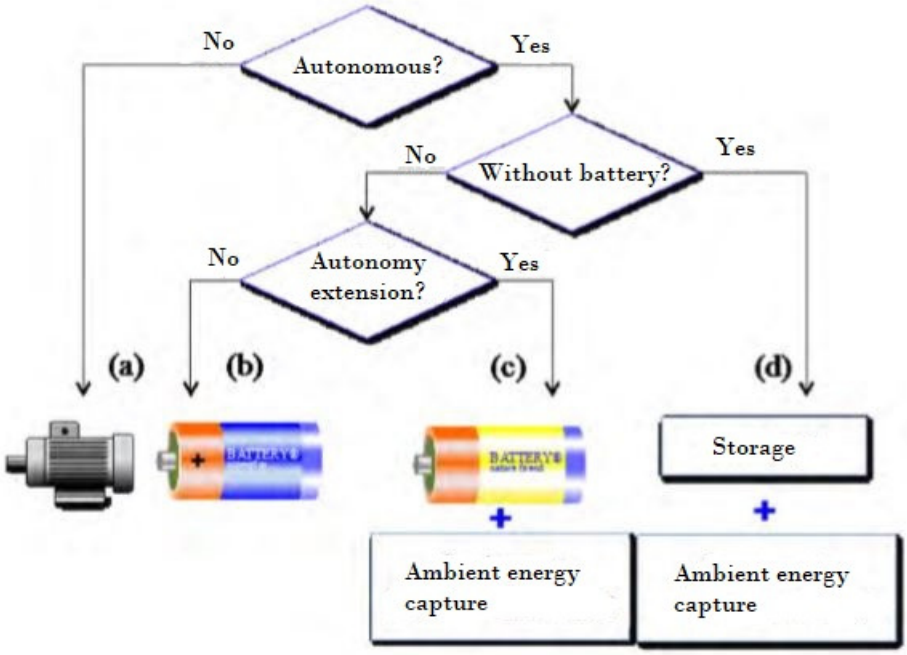

Figure 1.3: Choices for powering an autonomous node (a) wireline solution, (b) electrochemical storage, (c) electrochemical storage + autonomy extension, (d) ambient recovery only [2]

1.2 Wave Energy harvester buoy

1.2.1 A state-of-the-art review on wave energy harvesting

The first studies on alternative energy began shortly after the 1973 oil crisis. This geopolitical crisis saw the first peak in the oil price and had now been followed by several geopolitical as well as environmental crisis (see Fig.1.4). The use of renewable energies, which do not emit greenhouse gases, is becoming an economic, technological and political priority. Thus, for a number of years, all kinds of renewable energies have emerged: solar energy, wind energy, hydropower, geothermal energy and wave energy.

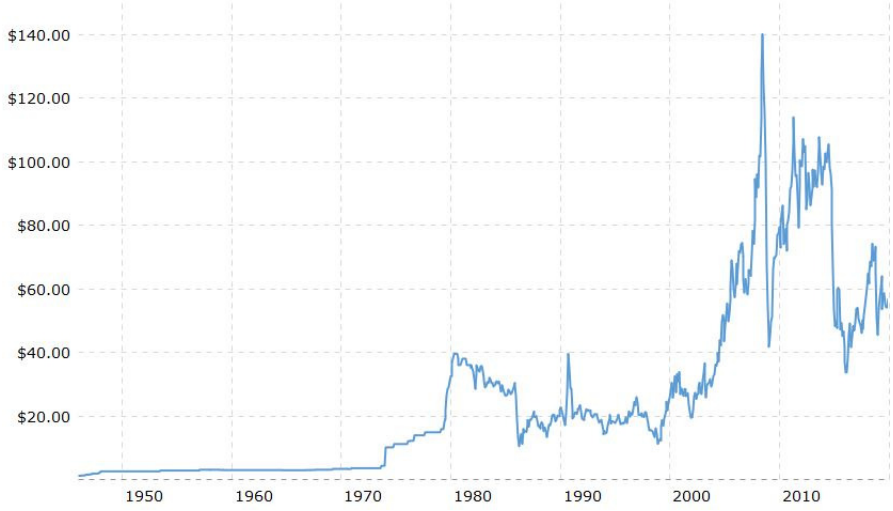

Figure 1.4: Non inflated oil price per barrel over the last 50 years (from macrotrends.net)

This source of energy actually originates from the wind. When wind blows near the ocean, part of the released energy is transmitted to the sea, creating waves that are all the greater as the wind is strong and over a long period of time. In addition to being free and renewable, this energy also has the advantage of being efficiently transmitted to the coast, even over distances of several thousand kilometres. Fig.1.5 illustrates the enormous potential that wave energy harvesting represents.

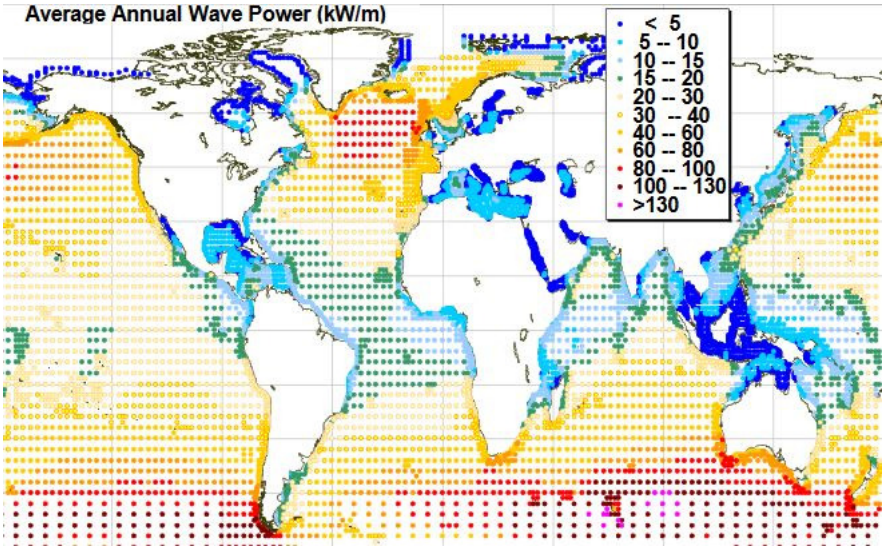

Figure 1.5: Global annual mean wave power estimates in kW/m [3]

In this section are presented some of the most important milestones in the development of wave energy conversion. Some of the solutions cited below are currently commercialized and offer perspectives on the modelling of our considered system.

– **Salter's duck**: The Salters duck, designed in the 1970s, is the first example of wave powering. Its principle is to use watertight boxes of asymmetrical shape rotating around an axis by operating hydraulic pumps. This principle has encountered many technological difficulties, particularly related to the holding of a long axis in the face of waves. Salter's duck remains today the pioneer of wave powering systems.

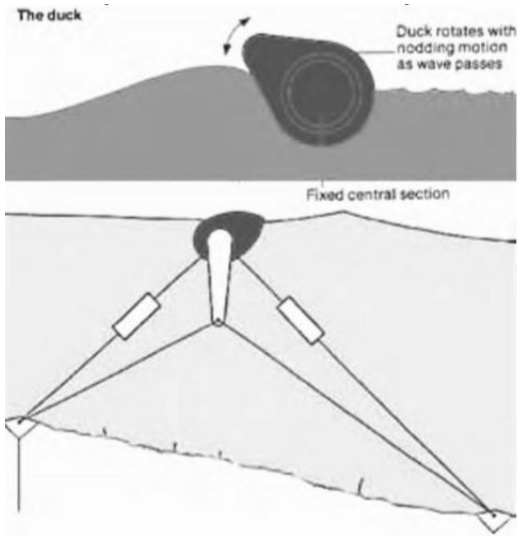

Figure 1.6: Salter's duck [4]

– **Power Buoy (Ocean Power Technologies, Inc., USA)**: This submerged buoy has a fixed part with tensioned anchor and an other part oscillating to the rhythm of the swell. The relative movement is dampened to be converted into electricity. This system, whose natural frequency makes its performance very sensitive to the wave period, requires specific control to maximize energy extraction, including predictive behaviour. The conversion device consists of a hydraulic pump, accumulator and motor driving an electric generator. Versions with direct linear electromagnetic generator are also being studied. Over a 20,000 m^2 area, 40 250 kW buoys would allow the installation of a 10 MW production capacity.

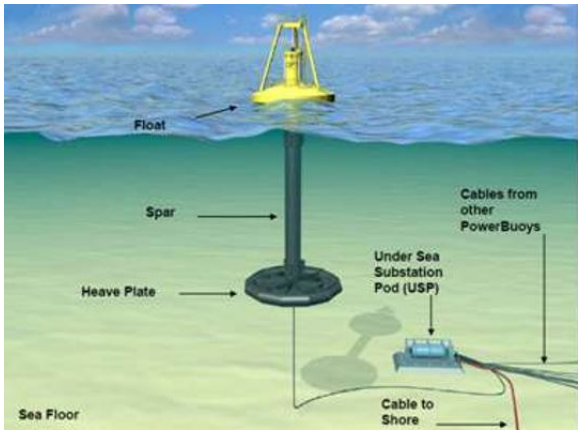

Figure 1.7: Principle of operation of the PowerBuoy [5]

– **Archimedes Wave Swing (AWS, Netherlands)**[12]: The pilot version, tested in 2004 off the coasts of Portugal, has a nominal power of 1 MW (cycle average) and a peak power of 2 MW. A cylindrical float is oscillated by the waves and compresses the air trapped between itself and a cylinder anchored at the bottom. It drives the moving part of a direct linear synchronous magnet generator. Thanks to an electronic power converter and appropriate control, the system makes it possible to exploit wave periods of between 9 and 20 seconds in an optimal way. The commercial version is planned with a diameter of 12 m, a maximum stroke of 12 m and an average power of 4.75 MW.

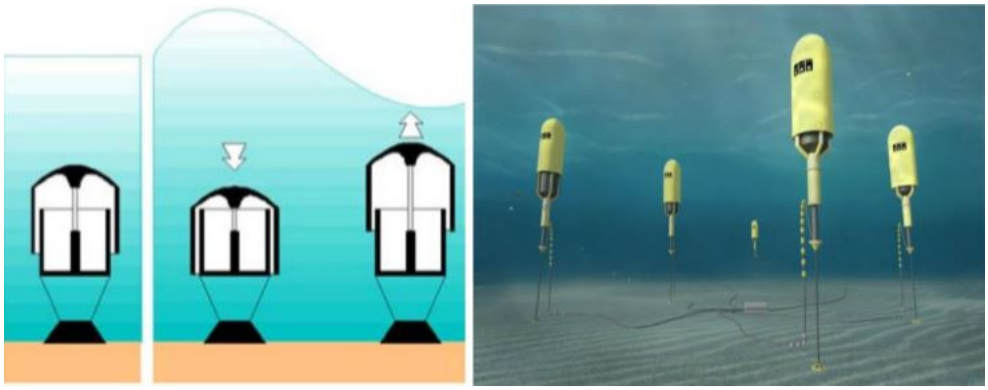

Figure 1.8: Archimedes Wave Spring principle and design [6]

– **Searev (a project led by the Ecole Centrale de Nantes)** : The Searev concept consists of a completely closed float inside which a pendulum weight is oscillating from the indirect stresses of the swell. In the prototype version, hydraulic cylinders dampen the pendulum and charge the accumulators. A real-time mechanical control, controlled by on-board computer technology, maintains the pendulum system in a state of parametric resonance despite the irregular nature of the excitation due to the waves. Hydraulic motors drive asynchronous generators with a maximum power of 500 kW. An all-electric solution with direct drive is also under study [13].

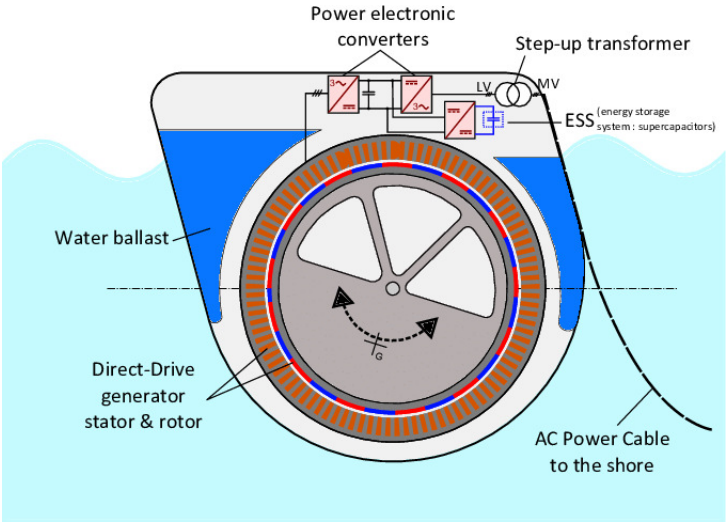

Figure 1.9: Principle of the SEAREV [7]

1.2.2 Proposed system

The proposed system (see Fig.1.10) is a cylindrical buoy powered by a linear inertial permanent magnet linear generator acting as a Power Take Off (PTO) mechanism. The PTO is made of a translator containing permanent magnets and a stator containing coils of wire. Upon action of the swell, the translator's mass will react to the heave motion of the buoy and will generate power.

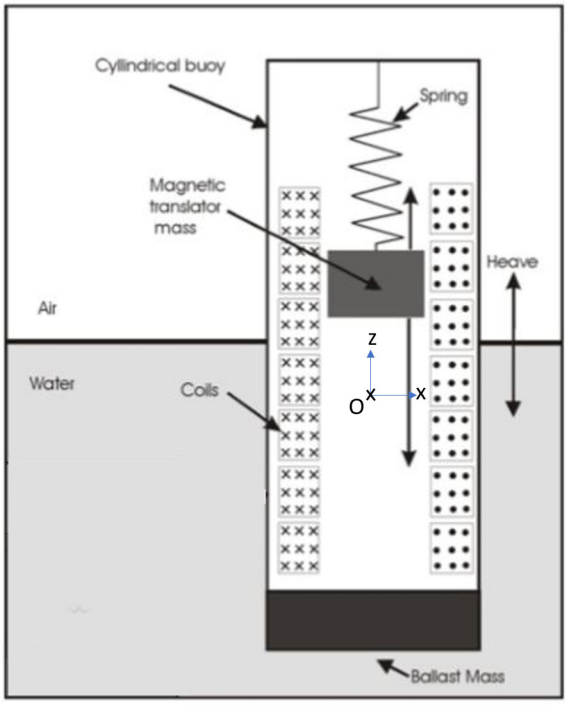

Figure 1.10: Scheme of the cylindrical buoy [8]

To ensure the verticality of the buoy in the water, it is equipped with a ballast mass on its bottom part. The choice of a cylindrical shape was made for simplification of calculation and reduction of computational time during simulations.

1.2.3 The problem with pitch instability

Power is extracted from the relative motion of the buoy and the magnets in the translator. The heave motion of the buoy is therefore the one that generates the most energy and is the one sought for. But in practice, parametric resonance induced by the sea swell converts a large part of the buoy's heave motion into pitch motion. This lowers the PTO efficiency while making the buoy and its antenna unstable, leading to poor or

even interrupted communication quality and data losses.
A solution to the issue of data losses was proposed in [14], using a retransmission mechanism based on mass storage and time division multiplexing, where the Buoy's communication terminal stores the real-time data that it transmits and can in the case of data losses, automatically or on-demand transmit the lost data to the base station.

1.3 Outline, objectives of the project

As discussed in section 1.2.3, the main practical issue in using a wave powered sensor buoy is the unwanted pitch motion caused by parametric resonance. It is a two-fold problem, reducing the power capture of the wave energy harvester and detrimentally affecting the data transmission of the wireless sensor node due to antenna misalignment. Previous research [8] was based upon linear numerical models, enabling frequency domain analysis and design optimization. However, parametric resonance causing the pitch motion is unable to be captured by linear modelling techniques.

The objective of this research will therefore be to extend the linear modelling and analysis performed in the previous research into a nonlinear framework capable of including the effects of parametric resonance.

2 An insight on Resonance and Parametric Resonance

This chapter covers some resonance phenomena occurring in oscillating systems and aims at providing an insight on parametric resonance, from the conditions of occurrence to direct applications.

2.1 Forced oscillations: linear and nonlinear cases

When an oscillator is excited by an external influence represented by a periodic time function in its differential equation of motion, its oscillations are called **forced**. For a linear mass-spring damper system, such differential equation can be written:

$$m\ddot{x} + b\dot{x} + kx = F_o cos(\omega t) \tag{2.1}$$

Where:

- m is the mass
- b the linear damping coefficient
- k the linear stiffness coefficient of the system
- F_o the amplitude of the periodic influence
- ω its pulsation

The general solution of such equation is composed of a homogenous $x_h(t)$ and a particular $x_p(t)$ solution, written as:

$$x(t) = \underbrace{C_1 e^{(-\frac{b}{2m}+\sqrt{(\frac{b}{2m})^2-\frac{k}{m}})t} + C_2 e^{(-\frac{b}{2m}-\sqrt{(\frac{b}{2m})^2-\frac{k}{m}})t}}_{x_h(t)} + \underbrace{X cos(\omega t - \theta)}_{x_p(t)} \tag{2.2}$$

Or:

$$x(t) = C_1 e^{(-\lambda+\sqrt{\lambda^2-1})\omega_n t} + C_2 e^{(-\lambda-\sqrt{\lambda^2-1})\omega_n t} + X cos(\omega t - \theta) \tag{2.3}$$

Where:

- C_1 and C_2 are determined for initial conditions

– X is the amplitude of the response:

$$X = \frac{F_o}{\sqrt{(k - m\omega^2)^2 + b^2\omega^2}} \tag{2.4}$$

– θ is the phase angle:

$$\theta = arctan\left(\frac{b\omega}{k - m\omega^2}\right) \tag{2.5}$$

– $2\lambda = \frac{b}{m}$ is the damping coefficient

– $\omega_n = \sqrt{\frac{k}{m} - 2\lambda^2}$ is the resonance pulsation

A resonance phenomenon is observed when w approaches w_n. Fig.2.1 illustrates the response of such system.

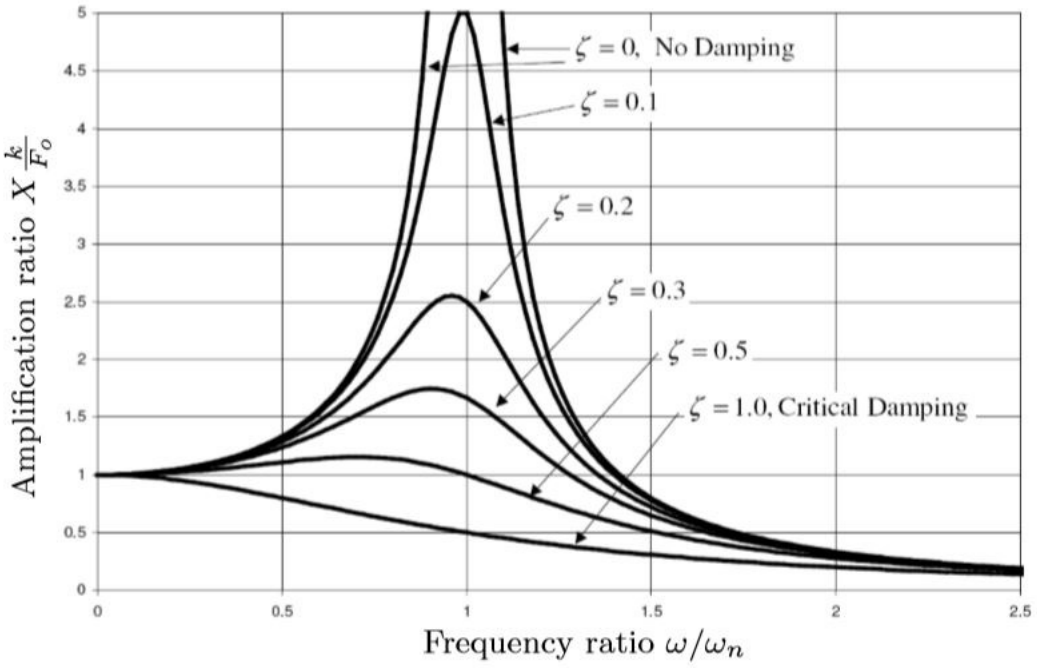

Figure 2.1: Resonance in a harmonically excited oscillator [9]

The frequency response of an oscillator is greatly altered when nonlinear phenomena are taken into consideration.
Consider a mass-spring damper system, with linear damping and a nonlinear cubic

stiffness k'. Its differential equation of motion can be written as:

$$m\ddot{x} + b\dot{x} + kx + k'x^3 = F_o cos(\omega t) \tag{2.6}$$

Such equation is called a Duffing equation [15]. By means of convenience, Eq.(2.6) is often re-written as follows [10]:

$$m\ddot{y} + 2\xi\dot{y} + y + \alpha y^3 = cos(\Omega\tau) \tag{2.7}$$

Where:

$$\begin{aligned} y &= \frac{x}{x_0} \\ \alpha &= \frac{k'x_0^2}{k} \\ \xi &= \frac{b}{2m\omega_0} \\ \omega_0 &= \sqrt{\frac{k}{m}} \\ \tau &= \omega_0 t \\ \Omega &= \frac{\omega}{\omega_0} \end{aligned} \tag{2.8}$$

With the displacement $x_0 = \frac{F_0}{k}(k' = 0, \omega = 0)$. The term α represents the ratio of the force due to the nonlinear stiffness, to the force due to the linear stiffness at x_0. Plus, when the amplitude of the force increases, α increases and y decreases. Changes in the value of α can therefore represent changes in the degree of non linearity of changes in the amplitude of the excitation force.

For such system, the resonance frequency shifts down if $k' < 0$ (softening system) and shifts up if $k' > 0$ (hardening system) compared to the linear case where k'=0. An increase in the amplitude of excitation tends to bend the response curve away from the linear case. Fig.2.2 illustrates the response of a Duffing oscillator. The dashed lines represent unstable solutions, characterised by a jump-up or a jump-down of frequency that occur when ω is slowly decreased or increased.

In most cases, nonlinear systems represented by equations such as the Duffing equation do not admit exact solutions. Numerical methods, such as the Homotopy Analysis Method ([16], [17]), the Differential Transform Method [18] or the Runge-Kutta Method [19] can be used to obtain approximated solutions.

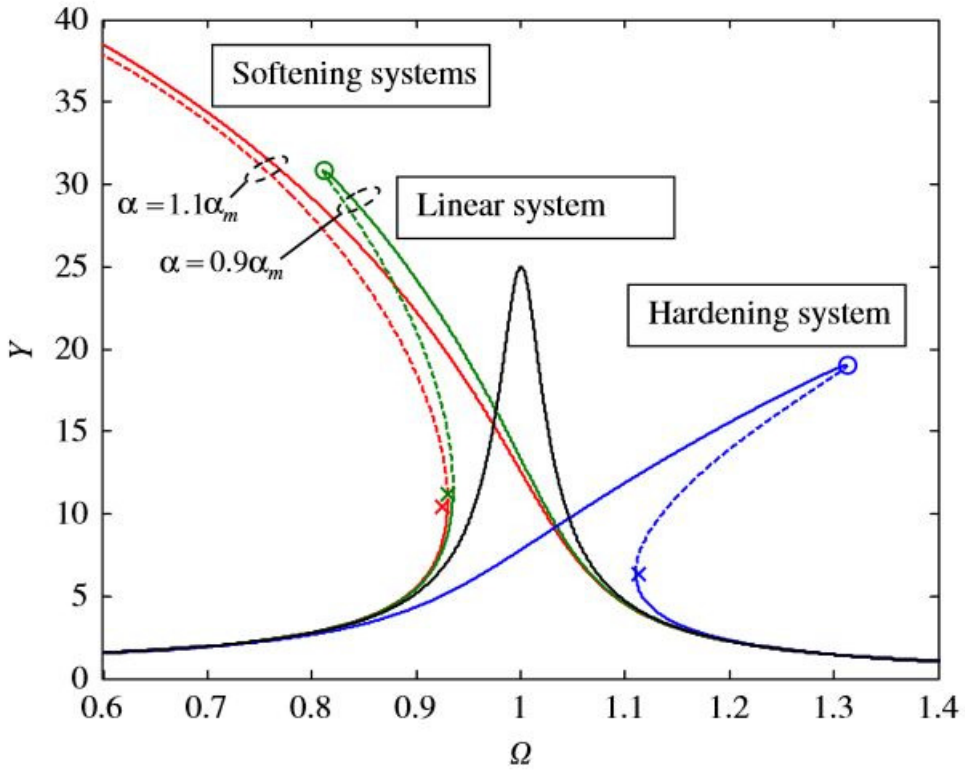

Figure 2.2: Frequency response curve for the Duffing oscillator [10]

2.2 Parametric resonance

2.2.1 Outline

Some oscillating systems are characterized by a periodic variation of one or several of their parameters. Such systems are described by differential equations in which time-varying coefficients appear, and are called parametrically excited systems. Situations occur where such systems become unstable, the periodic modulation of some parameter increasing steadily and causing a resonant increase in the amplitude of oscillation, with final state depending on the level of damping of the system. Such phenomenon is called a **parametric resonance**.

Parametric resonance phenomena occur in many systems, from the well known elastic pendulum [20] to motorcycles [21]. In the second half of the 19^{th} century, Froude was the first to study parametric resonance on ships ([22], [23]), observing large roll oscillations in cases where the frequency of oscillation in heave and pitch was approximately twice the natural roll frequency of the ship. In the 20^{th} century, marine researchers studied

more this phenomenon ([24], [25], [26]) and it later became a major field of research after the severe damage and losses on the APL China container ship in 1998 (see 2.2.3 and [27]).
In more recent years and coupled with the development of more efficient numerical techniques, parametric resonance applied to WECs has been the subject of many studies ([28], [29], [30], [31]).

2.2.2 Mathematical and Empirical conditions

Conditions supporting the apparition of parametric resonance have first been observed empirically [22]. The causes of parametric resonance and its behaviour differ greatly from those appearing in forced oscillations. For instance, parametric resonance can occur without any external force exciting the system. In the case of ship roll motion, parametric resonance may be triggered when some of the following conditions are met:

1. The period of the encounter wave is approximately equal to half the roll natural period
2. The wave length and ship length are approximately equal
3. The ship's roll damping is low

In general, parametric resonance is considered to be most triggered and of highest response when the frequency of parametric modulation is twice the natural frequency of the system (condition 1). In the model presented in Sect. 5 and 6, this condition will be the one taken into considerations.
It is to be noted that in damped systems, a treshold value of the amplitude of modulation of the parameter must be exceeded for parametric resonance to appear.

Parametrically excited systems are often described via the Mathieu equation([32], [33]). Such equation can be written as:

$$m\ddot{x} + b\dot{x} + k(t)x = 0 \tag{2.9}$$

Or after dividing by the mass:

$$\ddot{x} + \gamma\dot{x} + (\omega_n^2 + \beta cos(\omega t))x = 0 \tag{2.10}$$

Where:

– m and b are the mass of the system and a damping parameter (b constant and positive)

– $k(t) = k + acos(\omega t)$ is a time-varying harmonic restoring coefficient. k, a and ω are constant and positive

–
$$\gamma = \frac{b}{m} = 2\xi\omega_n \text{ and } \beta = \omega_n^2 \left(\frac{a}{k}\right) \tag{2.11}$$
With ω_n the natural frequency of the system and ξ the damping ratio

One more convenient formulation is obtained with the change of variable $\tau = \omega t$:

$$\frac{d^2x}{d^2\tau} + \kappa\frac{dx}{d\tau} + (\delta + \epsilon cos(\tau))x = 0 \tag{2.12}$$

Where:

$$\begin{aligned} \kappa &= 2\xi \left(\frac{\omega_n}{\omega}\right) \\ \epsilon &= \frac{\beta}{\omega^2} \\ \delta &= \left(\frac{\omega_n}{\omega}\right)^2 \end{aligned} \tag{2.13}$$

The Mathieu equation can have stable or unstable solutions, depending on the value of κ, ϵ and δ. Fig.2.3 shows the stability chart of the Mathieu equation (called Strutt-Ince diagram, see [34]) for κ=0, 0.1 and 0.2. It is to be noted that for $\kappa < 0$ the solution is always unstable.

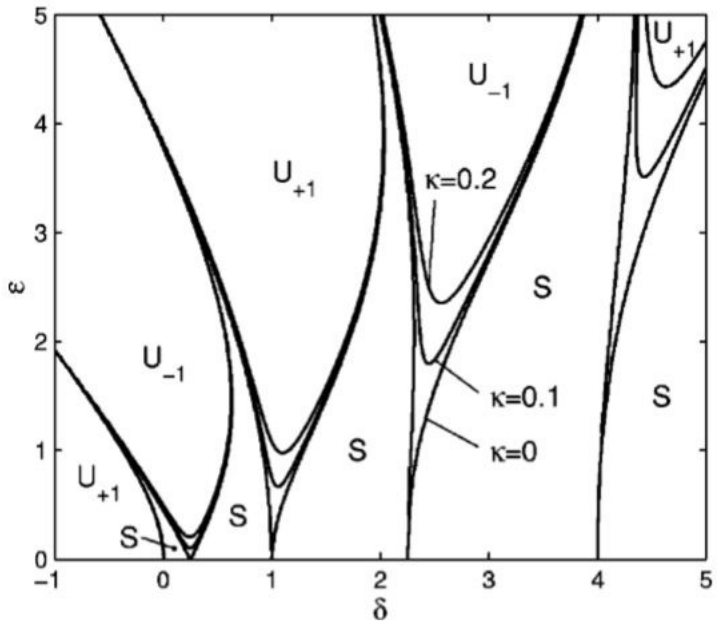

Figure 2.3: Mathieu stability chart for κ=0, 0.1, 0.2. Regions denoted S and U are respectively regions of stable and unstable solutions

2.2.3 Parametric resonance in marine structures: container ships accidents

In October 1998, the container ship APL China was on its way from Kaohsiung to Seattle when it was caught in a severe storm in the North Pacific. He was subjected to the storm for about 12 hours. The captain reduced speed and tried to steer in an ever heavier sea from the starboard bow. The watch officers later testified of sea conditions reaching the bridge (about 30 metres). The extreme bays collapsed and then those in the middle (there was a deck load of 1,300 containers). But according to experienced officers, what had most affected them were the sudden movements of the ship at the worst of the storm. Swings of 30° to 40° made handling impossible, the overspeed of the main engine associated with heavy ballast strikes reflected high pitch amplitudes. The roll heel occurring during extreme pitch reached angles of 40°.

The captain later stated that the ship was completely out of control at the worst of the storm. The morning after that, the damage was assessed: 400 of the 1,300 containers on the deck were drifting, 400 others had sustained extensive damage, and several were hanging along the ship's walls held by their seizure devices. Upon arrival at the port of Seattle, insurers and their experts estimated the amount of damage at $100 million. This was the highest amount of compensation paid for a container ship.

Figure 2.4: Damages on the containeurs. On the left, the APL China, on the right, the Dirch Maersk.

In January 2002, the container ship Dirch Maersk suffered similar damage during a crossing of the North Atlantic, followed by other vessels (OOCL America, P&O Nedloyd) in recent years. All captains report in their sea reports on the violence and unusual amplitude of the ship's movements.

3 1 Degree of Freedom analytical model

3.1 Framing

3.1.1 Hypothesis, notations

The considered system is a floating cylinder linked to a PTO device generating energy from the cylinder motion. The water is supposed to have infinite depth under the cylinder. We only consider heave motion for this first model. The buoy is described in a frame $R_0(0, x, y, z)$ and has a displacement ξ over the z axis. The origin of R_0 is given by the hydrostatic equilibrium of the buoy.

3.1.2 Equation of motion

We assume the fluid to be inviscid and the incident flow to be irrotational and incompressible [35]. The general displacement of the body $\xi(z,t)$ from its hydrostatic equilibrium position is given by Newton's second law:

$$m\ddot{\xi}(\mathbf{t}) = \mathbf{F_g} - \int\int_{S(t)} P(t)\mathbf{n}dS + \mathbf{F_{PTO}} \tag{3.1}$$

Where:

- m is the total mass of the body
- $\mathbf{F_g} = -mg\mathbf{z}$ represents the gravity force with g the acceleration of gravity
- S is the submerged surface
- P is the pressure
- $\mathbf{n} = (n_x, n_y, n_z)$ is a vector normal to the surface
- $\mathbf{F_{PTO}}$ represents the power take-off forces

3.2 Modelling the fluid forces

3.2.1 Theoretical background

The torsor of hydrodynamic forces generated by the presence of the body in the water is the sum of the pressures expressed in the reference frame R_0, by means of the Bernoulli

equation:

$$P(t) = -\gamma g z(t) - \gamma \frac{\partial \phi(t)}{\partial t} - \gamma \frac{|\nabla \phi(t)|^2}{2} \tag{3.2}$$

Where:

- $\phi(t) = \phi_I + \phi_D + \phi_R$ is the potential flow
- ϕ_I, ϕ_D, ϕ_R are respectively the incident flow, diffraction and radiation potentials

From equation (2) and the definition of the potential flow, we can identify different forces acting on the body:

- **Excitation forces**: The disturbances due to the presence of the body on the incident wave field are neglected. This implies retaining in the exciting forces only the components due to the deformation of the undisturbed free surface and the incident flow potential. This approximation defines Froude-Krylov efforts.
  The formulation of Froude-Krylov efforts reveals two terms. The first, corresponding to the torsor of the hydrostatic eorts is obtained by integrating the hydrostatic pressure on the instantaneous wet surface. Thereafter we also consider that it contains gravity forces. The second highlights the dynamic pressure of the incident field, which is also applied to the instantaneous wetted surface of the body. Therefore the following forces are considered:
  - $\mathbf{F_{FK_{st}}}$ is the static Froude-Krylov force:

$$\mathbf{F}_{FK_{st}} = \mathbf{F_g} + \int\int_{S(t)} -\gamma \mathbf{n} dS \tag{3.3}$$

  - $\mathbf{F_{FK_{dy}}}$ is the dynamic Froude-Krylov force:

$$\mathbf{F}_{FK_{dy}} = -\int\int_{S(t)} P_{dy} \mathbf{n} dS \tag{3.4}$$

    where $P_{dy} = -\gamma \frac{\partial \phi_I(t)}{\partial t} - \gamma \frac{|\nabla \phi_I(t)|^2}{2}$ is the dynamic pressure

- $\mathbf{F_D}$ is the diffraction force:

$$\mathbf{F}_D = -\int\int_{S(t)} P_D \mathbf{n} dS \tag{3.5}$$

  where $P_D = -\gamma \frac{\partial \phi_D(t)}{\partial t} - \gamma \frac{|\nabla \phi_D(t)|^2}{2}$ is the diffraction pressure

– $\mathbf{F_R}$ is the radiation force:

$$\mathbf{F}_R = -\int\int_{S(t)} P_R \mathbf{n} dS \tag{3.6}$$

where $P_R = -\gamma \frac{\partial \phi_R(t)}{\partial t} - \gamma \frac{|\nabla \phi_R(t)|^2}{2}$ is the radiation pressure

Combining these equations, we can rewrite the equation of motion of the buoy:

$$m\ddot{\xi} = \mathbf{F}_{FK_{st}} + \mathbf{F}_{FK_{dy}} + \mathbf{F}_D + \mathbf{F}_R + \mathbf{F}_{PTO} \tag{3.7}$$

3.2.2 Modelling approaches

The waves are considered to be linear and the quadratic terms of the potential equation neglected.
For wavelengths much larger than the dimensions of the buoy, nonlinearites of Diffraction and Radiation can be neglected ([36] and [37]). When both nonlinear Froude-Krylov and Radiation/Diffraction forces are implemented on a heaving point absorber [38], the dynamic response of the device shows that the effect of Diffraction and Radiation nonlinearities is negligible in comparison to the Froude-Krylov forces.
Only two modelling approaches are therefore considered: one with Froude-Krylov forces linearised and one taking into account their nonlinearity.

3.2.2.1 Linear Froude-Krylov

For waves of small steepness and amplitude, the flow potential is linearised [35]. Hydrodynamic forces are integrated over the mean wetted surface of the buoy S_M. The equation of motion becomes:

$$m\ddot{\xi} = \underbrace{-k_H \xi}_{F_{FK_{st}}} \underbrace{- \int_{-\infty}^{+\infty} k_{Ex}(t-\tau)\eta(\tau)d\tau}_{F_{Ex}=F_{FK_{dy}}+F_D} \underbrace{- \mu_\infty \ddot{\xi} - \int_{-\infty}^{+\infty} k_R(t-\tau)\dot{\xi}(\tau)d\tau}_{F_R} \underbrace{- C_{PTO}\dot{\xi}}_{F_{PTO}} \tag{3.8}$$

Where [39]:

– $\mathbf{F_{FK_{st}}} = -k_H \xi$: acts like a mass-spring system, with an hydrostatic stiffness k_H.

Static Froude-Krylov forces represent both gravity and Archimedes forces acting one against the other on the device.

- $\mathbf{F_{Ex}} = -\int_{-\infty}^{+\infty} k_{Ex}(t-\tau)\eta(\tau)d\tau$: represents both dynamic Froude-Krylov and diffraction forces. k_{Ex} is the excitation impulse-response function (IRF). The excitation force is calculated using the convolution product between k_{Ex} and the free-surface elevation η.
- $\mathbf{F_R} = -\mu_\infty \ddot{\xi} - \int_{-\infty}^{+\infty} k_R(t-\tau)\dot{\xi}(\tau)d\tau$: is expressed by the added mass μ_∞ and the convolution between the radiation IRF k_R and the velocity $\dot{\xi}$, using Cummins decomposition [40].
- $\mathbf{F_{PTO}} = -C_{PTO}\dot{\xi}$: is modelled as a linear damper using a fixed damping coefficient C_{PTO}.

3.2.2.2 Nonlinear Froude-Krylov

In this section, Froude-Krylov forces are computed by integration over the instantaneous wetted surface. The wetted surface is re-defined at each time-step and its calculation is much more computationally expensive but is expected to give finer results since the nonlinearities of Froude-Krylov forces should play a major role in the motion of the buoy.
Using this new model, the equation of motion can be re-written as:

$$m\ddot{\xi} = F_g - \int\int_{S(t)} (P_{st}+Pdyn)ndS - \int_{-\infty}^{+\infty} k_D(t-\tau)\eta d\tau - \mu_\infty\ddot{\xi} - \int_{-\infty}^{+\infty} k_R(t-\tau)\dot{\xi}(\tau)d\tau - C_{PTO}\dot{\xi} \tag{3.9}$$

Where:

- Froude-Krylov forces are integrated over the instantaneous wetted surface.
- The diffraction force is calculated using the convolution product between k_D and the free-surface elevation η.
- The radiation force and power-take off force are calculated the same way as in the linear approach.

3.2.3 Algebraic integration of the Froude-Krylov forces

In this section, a computationally efficient algebraic integration of the Froude-Krylov forces is operated. Such method is valid for vertical axisymmetric buoys (when the body is pitching, numerical integration will be necessary).
The geometry of a buoy symmetric around a vertical axis, in cylindrical coordinates, is described as following:

$$\begin{cases} x(\sigma,\theta) = f(\sigma)\cos\theta \\ y(\sigma,\theta) = f(\sigma)\sin\theta \\ z(\sigma,\theta) = \sigma \\ \theta\epsilon[0,2\pi] \wedge \sigma\epsilon[\sigma_1,\sigma_2] \end{cases} \tag{3.10}$$

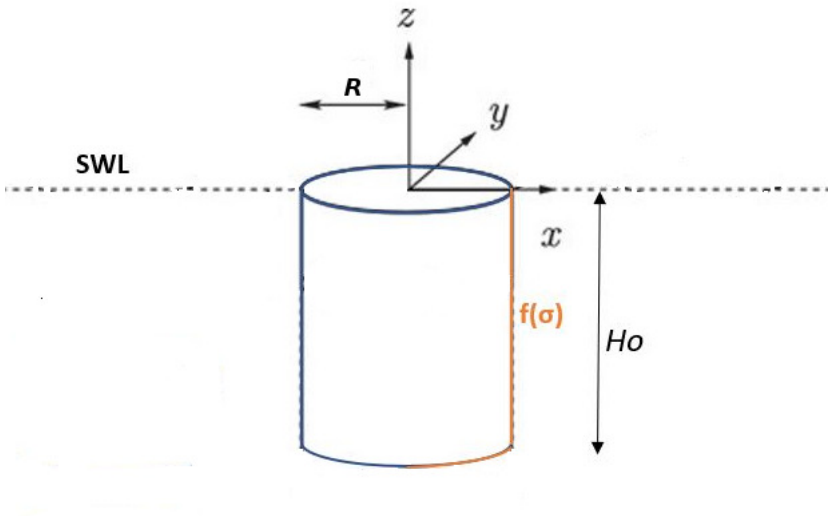

Figure 3.1: Axisymmetric vertical device with generic prole of revolution f(σ), at rest

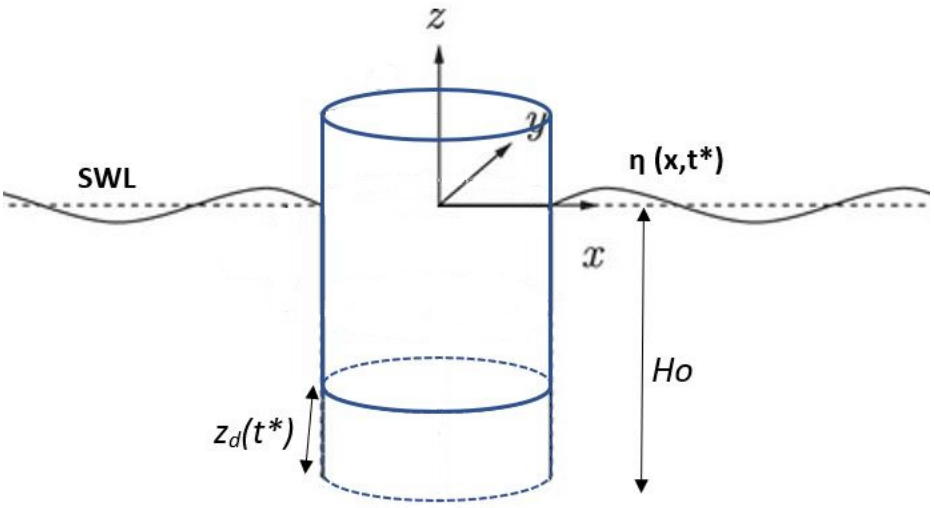

Figure 3.2: Axisymmetric vertical device showing the free surface elevation η and the displacement z_d

In cylindrical coordinates, the Froude-Krylov forces become:

$$F_{FK_{st}} = F_g + \int\int_{S(t)} -\gamma z n dS = F_g + \int_{\theta_1}^{\theta_2}\int_{\sigma_1}^{\sigma_2} -\gamma z(\sigma,\theta)(e_\sigma \times e_\theta)d\sigma d\theta$$

$$F_{FK_{dy}} = \int\int_{S(t)} p_{dy} n dS = \int_{\theta_1}^{\theta 2}\int_{\sigma_1}^{\sigma_2} p_{dy}(\sigma,\theta)(e_\sigma \times e_\theta)d\sigma d\theta$$

The cross product of the unity vectors, as well as the cross product for the torques, can be expressed as following:

$$e_\sigma \times e_\theta = \begin{pmatrix} f'(\sigma)\cos\theta \\ f'(\sigma)\sin\theta \\ 1 \end{pmatrix} \times \begin{pmatrix} -f(\sigma)\sin\theta \\ f(\sigma)\cos\theta \\ 0 \end{pmatrix} = f(\sigma)\begin{pmatrix} -\cos\theta \\ -\sin\theta \\ f'(\sigma) \end{pmatrix}$$

$$r \times (e_\sigma \times e_\theta) = \begin{pmatrix} f(\sigma)\cos\theta \\ f(\sigma)\sin\theta \\ \sigma \end{pmatrix} \times f(\sigma)\begin{pmatrix} -\cos\theta \\ -\sin\theta \\ f'(\sigma) \end{pmatrix}$$

σ_2 is set constant and equal to the free surface elevation of the buoy $\bar{\eta}$ at its axis.

This approximation is valid for horizontal dimensions of the buoy much shorter than the wave lengths. Considering that the buoy is deployed in deep-water location, the pressure formulation can also be assumed as in infinite water-depth.

4 Numerical techniques for 2 Degrees of Freedom

4.1 Objectives

Unlike well developed WEC devices such as the Archimedes Wave Swing which can be tested full scale, new concepts need to be undergoing numerical efficiency evaluation so that the designers can assess their viability in realistic wave conditions before investing a lot of time, effort and money into development.
Historically such evaluations have been conducted via frequency-domain models of the floating body response [37]. In the case of a single heave motion, the frequency domain analysis gives results sufficiently correlated to experimental measurements [41], whereas the correlation is poorer when surge and pitch are considered [42] [43]. This is mostly due to the fact that linear models consider small wave amplitude and body motion, while a pitching WEC usually requires its response to be resonant with the incoming waves, resulting in large amplitudes of motion to maximize the energy harvesting. A fully linear model can therefore be obsolete for such devices and other models have to be investigated.

4.2 A review of numerical techniques

This section reviews some of the most well known and used numerical techniques to model and control complex, partially of fully non-linear systems.

4.2.1 Boundary Element Method

The finite boundary element method (BEM) is a numerical technique developed since the early 1960s and based on the older theory of boundary integral equations. This theory dates back to the early 19th century with the works of Poisson (1820), Betti (1872) and Kirchhoff (1882) among others. It was only around 1960 that Jawson, Hess, Symm and others developed the finite element boundary method, the name BEM only appearing for the first time in the literature in 1977 [44]. BEM has since been the subject of numerous publications ([45], [46]) and still represents an important area of research, thanks in particular to the increasing power of the computers available. Particularly, the computational efficiency of this method compared to smoothed-particle hydrodynamics (SPH) or computational fluid dynamics (CFD) simulation methods makes BEM a widely preferred choice in early stage device development.
BEM is based on the potential theory. When a harmonic linear wave field encounters

a body, a scattering and a radiating velocity potentials arise [47]. BEM solves these potentials individually:

- The scattering potential is solved assuming that the waves encounter a fixed body. From this we can derive the exciting force F_{Ex} acting on the body.
- The radiating potential on the other hand is solved assuming a moving body in the absence of incident waves. Solving this allows to obtain the radiation force F_R containing the added mass μ_∞ and radiation damping coefficient k_R (see Eq.8)

This method has emerged as an alternative to the other major numerical method: the FEM (finite element method). BEM appears more appropriate in infinite space than FEM since only the surface of the boundary of the domain must be discretized.

4.2.2 Gain Scheduling

Gain scheduling is a powerful and widely used design methodology for engineering applications. It has particularly proven to be a successful method for the control of nonlinear systems ([48], [49]). This method exploits linear, well understood design control methods to describe and control the nonlinearities of a system, making it an interesting and efficient tool for many designers.
A linear structure of parametric variations (the interpolation of the nonlinearities of the system) forms what is called a Time-Varying Parameter (TVP) model [50]. Several operating points covering the range of the system's dynamic (heave and pitch motion in the present study) are selected. From each of these points is derived a Linear Time-Invariant (LTI) approximation on which a linear compensator is applied. The gains of the compensator are then interpolated (scheduled) in between the operating points to form a global compensator [48]. Fig.4.1 shows how a gain scheduled control is operated in a block diagram view.

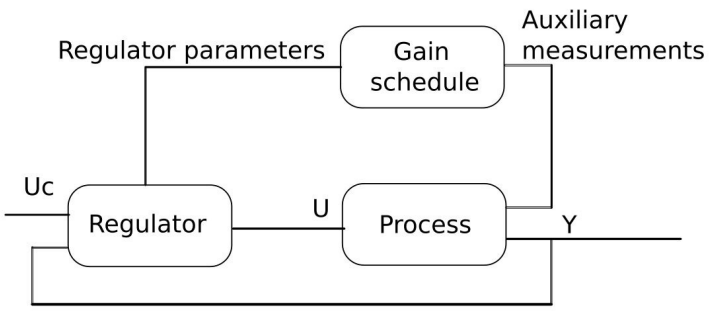

Figure 4.1: Block diagram of a system controlled by gain scheduling (from [11])

Gain scheduling originated in the development of flight control systems. The mach-number and the dynamic pressure were used as scheduling variables.

4.3 Application to the proposed model

In this study, BEM was chosen for the calculation of hydrodynamic coefficients. The NEMOH toolbox (see Sect 5.2) was adapted and used for this matter, in the MatLab environment. Calculations being computationally demanding, the coefficients were **pre-calculated** on a chosen range of positions of draught and pitch. Results of calculations for each pitch and draught position (including Excitation force, Restoring coefficient and Impulse Response Functions of added mass) were then separately saved and stored, to be loaded into look-up tables, allowing to **interpolate** the hydrodynamic data between these positions (see Sect. 5.3) and creating a time-varying parameter control model via Simulink.

5 2 DoFs numerical model: code and computation

5.1 Overview

In this section a description of the numerical model is presented. The geometry of the body, its considered motion and the modelled waves are discussed.

A cylindrical body is considered to be moving in heave and pitch in water. The PTO is not modelled here for simplification purposes. All calculations are done in the MatLab environment. Fig.18 shows the scheme of the cylinder.
The characteristics of the cylinder are the following:

- $R = 0.35$m : Radius of the cylinder
- H : Draught of the cylinder. The calculations are only done for the immersed part of the body. H, as well as the Pitch angle are varying parameter and the hydrodynamic coefficients are computed for a whole range of H and Pitch values.
- **Distribution of mass** : The Center of Mass (CoMz) is considered to be on the vertical axis of revolution, at $h = 0.75$m above the bottom of the cylinder. The mass is distributed in a full cylinder of height $2h$ with CoMz at its center. Therefore:

  $m = \pi R^2 H \rho$ is the mass of the body

  $I_{55} = \frac{m}{12}(3R^2 + (2h)^2)$ is the moment of inertia of the body on the Y axis

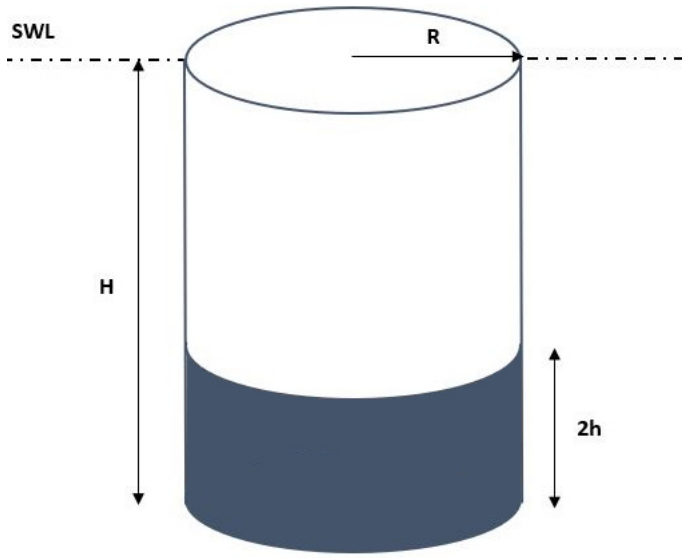

Figure 5.1: Mass distribution in the considered cylinder

The incoming waves are modelled as sinusoidal waves with parameters of amplitude and frequency which can be set for different calculations.

A mesh of the cylinder was created for the following range of positions:

- Draught position of -0.2m to -4.0m, with -0.2m increment
- Pitch position of -40°to +40°, with 10°increment

5.2 Obtaining hydrodynamic coefficients with the NEMOH toolbox

NEMOH is a BEM code designed for the calculation of first-order hydrodynamic coefficients. It has been developped at Ecole Centrale de Nantes (France) for 30 years. It was the first open source BEM code and is still used in many research projects. Its common use is to evaluate the dynamic response of floating structures or to evaluate the performance of wave energy converters [47].
The approach for obtaining hydrodynamic coefficients of a given geometry is threefold:

1. **Pre – processor**: Reads and prepares the mesh and calculation cases (sets of body conditions).

2. **Solver**: For each body condition, solves the Boundary Value Problem (BVP) of the potential. Calculates pressure field, hydrodynamic coefficients, far field coefficients and wave elevation.

3. **Post − processor**: Post-processes results, used to calculate Response Amplitude Operators (RAOs) and to plot the free surface wave elevation.

5.2.1 Pre-processor

5.2.1.1 Mesh generation

The aim of the pre-processor is to prepare the mesh and to generate the body conditions for each calculation case (radiation and diffraction). The inputs include body conditions (geometry of the mesh, number of panels of the mesh, number of DoFs to be analysed) and environmental values (water density, wave direction and frequency). NEMOH can generate meshes through two MatLab functions, axiMesh.m and Mesh.m, respectively used for axisymmetric and non-axisymmetric geometries. The meshes are composed of flat quadrilateral panels, as shown in Fig.5.2. For generating an axisymmetric mesh, only a few points of the contour of the geometry are necessary.

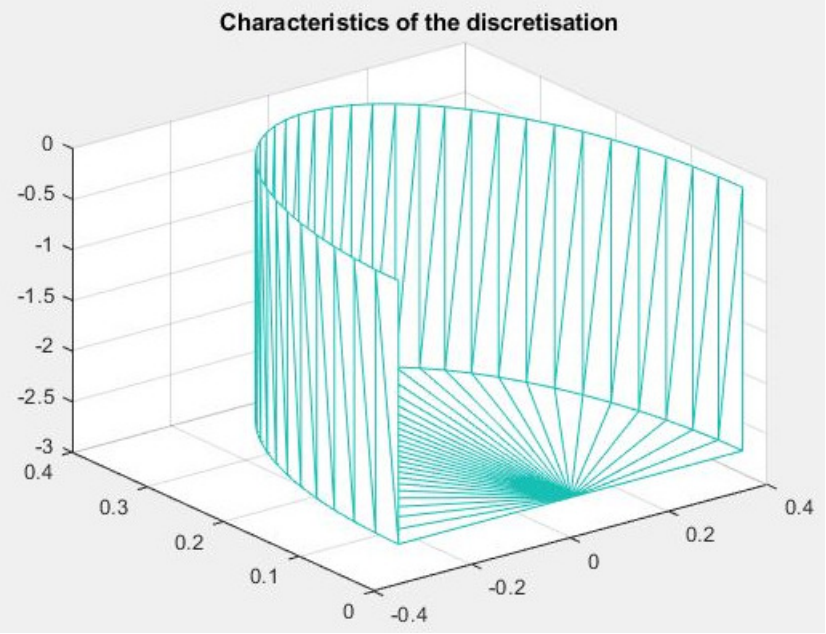

Figure 5.2: Discretised mesh for 2.6m draught and 0°pitch angle

Apart from the mesh characteristics, the pre-processor gives some other outputs used in the solver, among which:

– Normal velocities, i.e the body conditions for each radiation and diffraction problem

– Froude-Krylov forces for each diffraction problem

– Coordinate of the free surface, to calculate the wave elevation

5.2.1.2 Rotating the Mesh

From the axiMesh.m function was computed axiMeshRotate.m, which allows to generate meshes for pitched models, by rotating the points of contour of the original geometry. Consider the buoy being rotated (pitched) by an angle β in regards to its Center of Mass C. The buoy is described in a reference frame $R_0(0, X_0, Y_0, Z_0)$. Coordinates of C are $(X_C, 0, Z_C)$. A point M$(X_M, 0, Z_M)$ on the surface of the buoy will be transformed into N as following (see Fig.5.3 also):

$$\begin{cases} X_M - X_C = Rcos\alpha \\ Z_M - Z_C = Rsin\alpha \end{cases}$$

$$\begin{cases} X_N - X_C = Rcos(\alpha+\beta) = R(cos\alpha cos\beta - sin\alpha sin\beta) \\ Z_N - Z_C = Rsin(\alpha+\beta) = R(sin\alpha cos\beta + sin\beta cos\alpha) \end{cases}$$

$$\begin{cases} X_N = X_C + (X_M - X_C)cos\beta - (Z_M - Z_C)sin\beta \\ \\ Z_N = Z_C + (Z_M - Z_C)cos\beta + (X_M - X_C)sin\beta \end{cases} \tag{5.1}$$

We can therefore write the coordinates of a node i of the mesh for a pitch angle β $\eta_i^\beta(X_i^\beta, Y_i, Z_i^\beta)$, in regards to the same node at $\beta = 0°$:

$$\begin{pmatrix} X_i^\beta = X_C + (X_i^0 - X_C)cos\beta - (Z_i^0 - Z_C)sin\beta \\ \\ Y_i \\ \\ Z_i^\beta = Z_C + (Z_i^0 - Z_C)cos\beta + (X_i^0 - X_C)sin\beta \end{pmatrix} \tag{5.2}$$

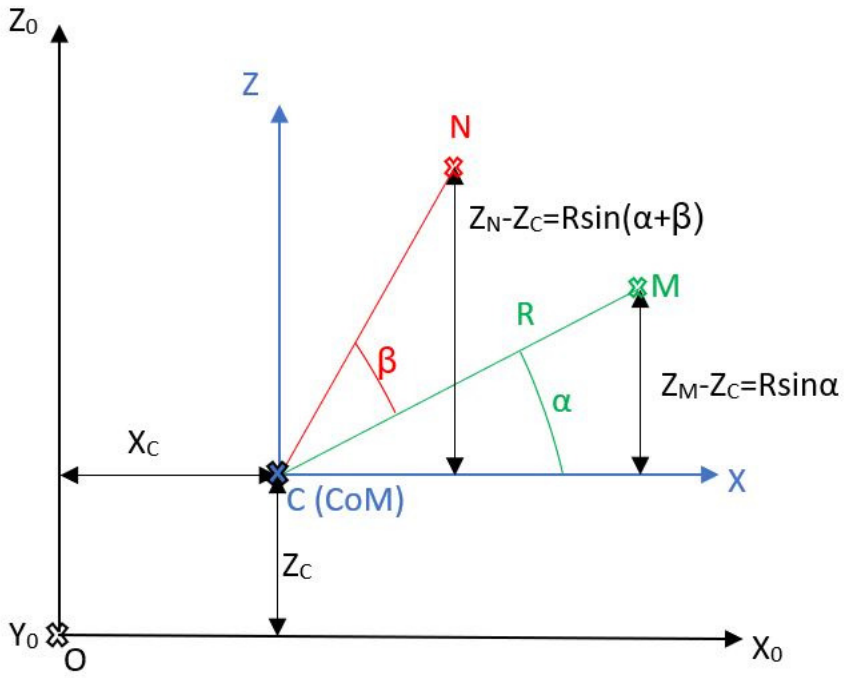

Figure 5.3: Rotation of angle β of the point M in regards to point C in R_0

Fig.5.4 shows the discretised mesh rotated by 20°, generated with axiMeshRotate.m, and cut above the still water level.

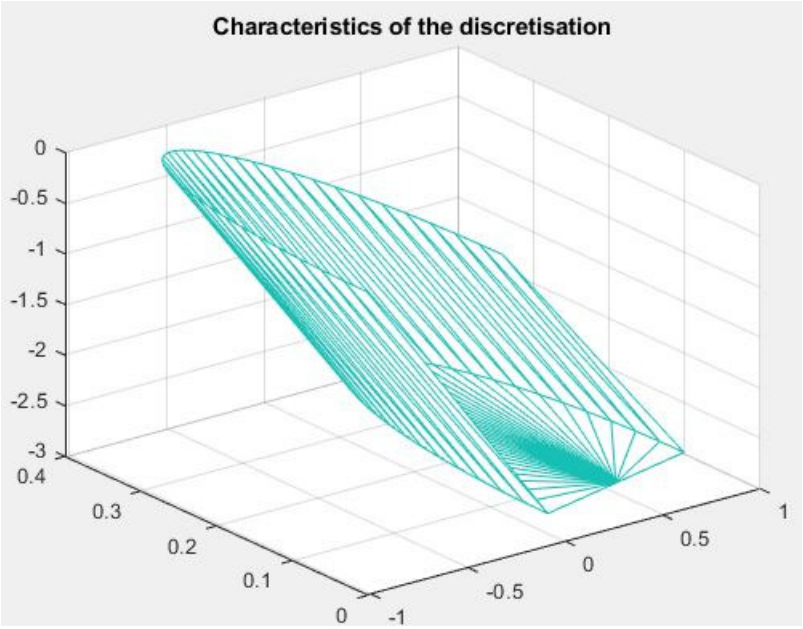

Figure 5.4: Discretised mesh for 2.6m draught and 20°pitch angle

5.2.2 Solver and post-processor

The solver and the post-processor respectively solve the linear BVP of each body condition for radiation and diffraction problems, and postprocess the results in terms of relevant quantities, such as added mass, radiation damping or excitation force.
After post-processing is done, the following results are given:

- Radiation coefficients, containing added mass and damping forces from the radiation problems
- Diffraction forces and Excitation forces from the diffraction problems
- Impulse Response Functions for the radiation force and infinite frequency added mass m_{inf}

5.3 Body response model

5.3.1 Outline: MatLab code, loading results from NEMOH

The body response model was computed on a *model_run* MatLab function. The full code is displayed on Appendix.
Inputs of the model include the cylinder description (radius, mass, inertia), initial conditions of position and description of the incoming waves: shape, amplitude, frequency. The code then loops through all considered positions and loads for each position the following calculation results from NEMOH:

- *Excite.mat*: These are the excitation force coefficients F_e, stored in a 300*6 matrix because NEMOH calculates excitation coefficients for 6 degrees of freedom. Since only Heave and Pitch motions are considered in the current study, F_e coefficients are separated into F_{e3} and F_{e5}, respectively columns 3 and 5 of the F_e matrix
- *w.mat*: Corresponding frequencies for the excitation coefficients (300*1 list)
- *KH.mat*: 6*6 matrix corresponding to the restoring coefficients calculated by NEMOH. From this, two matrixes KH_3 and KH_5 are created, corresponding respectively to the heave and pitch restoring coefficients, as 20*9 matrixes for 20 heave positions and 9 pitch positions
- *IRF.mat*: Gives the results the Impulse Response Function of added mass for heave and pitch, stored separately as single values $m_{infHeave}$ and $m_{infPitch}$

– *Heave_Rad_SS.mat*, *Pitch_Rad_SS.mat*: These are the State-Space parameters for the equilibrium position (zero heave, zero pitch)

As said in Sect. 4.3, The results of NEMOH calculations are interpolated between the considered range of positions. To do so, results of Excitation force, Restoring force and added mass were stored into lookup tables. For the coefficients of Radiation force, a State-Space model could be used, because of the linear approach of Radiation, as discussed in Sect. 3.2.2.

5.3.2 SIMULINK model detailed

5.3.2.1 Overall system

The skeleton of the SIMULINK model is described in Fig.5.5. It is composed of 4 subsystems, corresponding to Excitation and Restoring forces, Inertia (added mass) and the State-Space model for Damping coefficients.

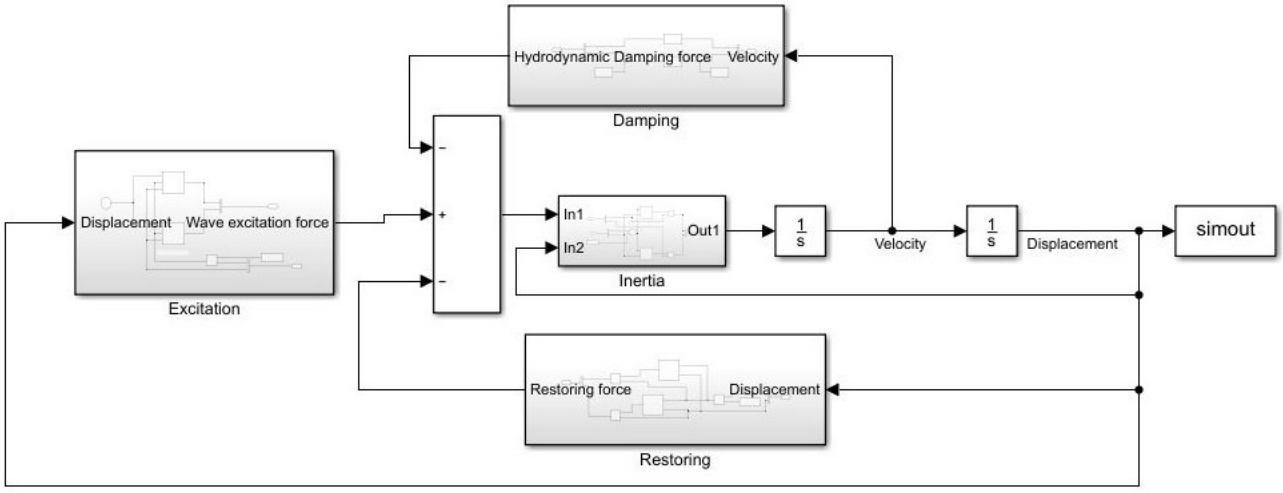

Figure 5.5: SIMULINK model skeleton

5.3.2.2 Subsystems containing lookup tables

Fig.5.6 to 5.8 describe the subsystems where lookup tables were used for interpolation of the NEMOH calculations. Details on the inputs of these lookup tables can be found in the MatLab code in Appendix.

Excitation Force

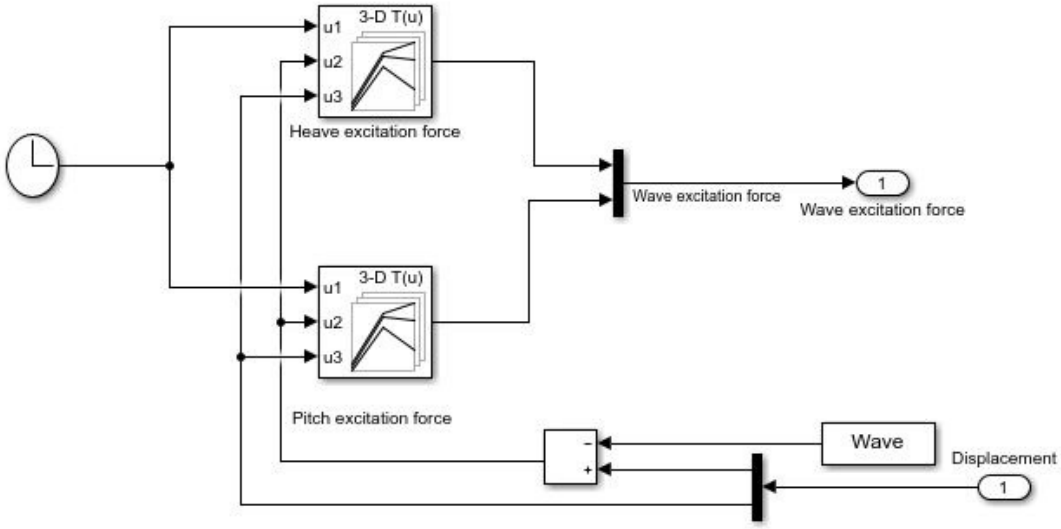

Figure 5.6: Excitation subsystem

Restoring force

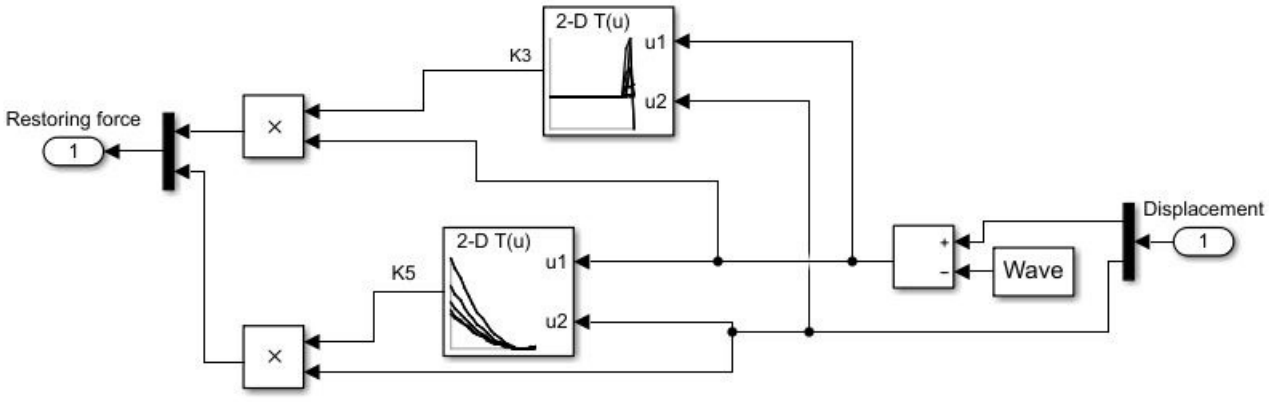

Figure 5.7: Restoring subsystem

Inertia

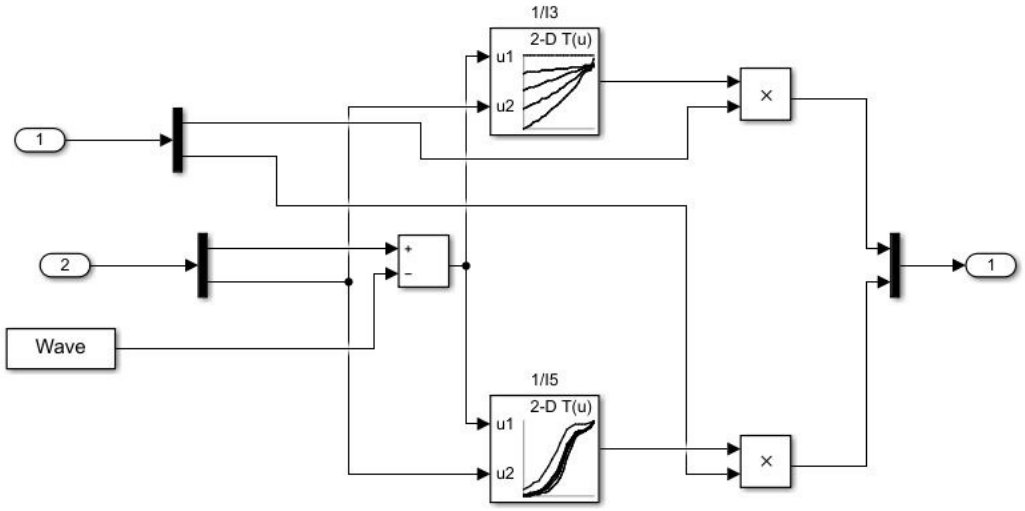

Figure 5.8: Inertia subsystem

5.3.2.3 State-Space model for the damping coefficient

The State-Space model was implemented by using $Heave\_Rad\_SS.mat$ and $Pitch\_Rad\_SS.mat$, containing the State-Space parameters A_{ss3}, B_{ss3}, C_{ss3} and D_{ss3} for heave damping, and A_{ss5}, B_{ss5}, C_{ss5} and D_{ss5} for pitch damping. Fig.5.9 describes this model.
The Finite Order Approximation by Moment-Matching (FOAMM) method was used to obtain the coefficients. Theory on this method and a toolbox can be found in [51] and [52].

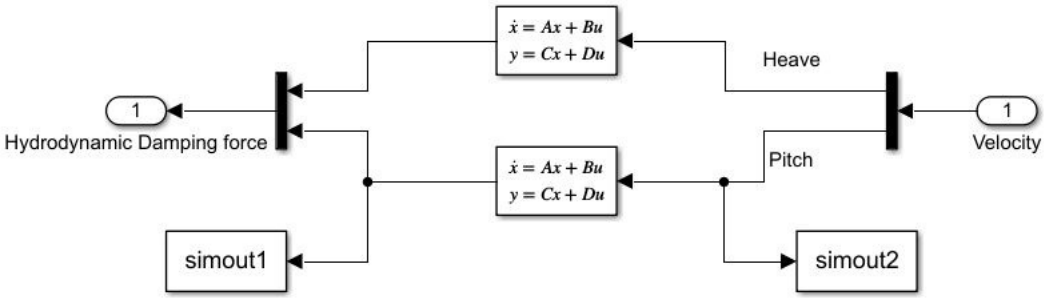

Figure 5.9: Damping subsystem

6 Results, discussions

In this section, results of the simulations operated with the *model_run* code are presented and discussed. As parametric resonance phenonema were looked for, the system entered states of very high amplitude of motion and some of the solutions diverge. Efforts were made to discuss the range and limits of the presented model.

6.1 Free decay test

Free decay tests were first operated in order to determine the natural heave and pith frequencies of the body. In these tests the cylinder is "released" from an initial position of draught or pitch, with no incoming wave and its oscillations are studied. Results of heave decay and pitch decay tests are shown in Fig.6.1 and 6.2.

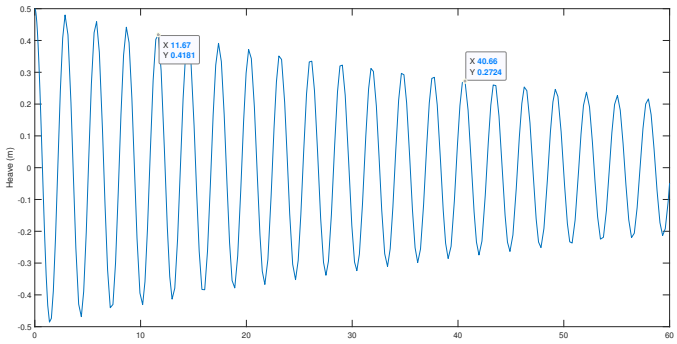

Figure 6.1: Heave decay test with initial position=0.5m

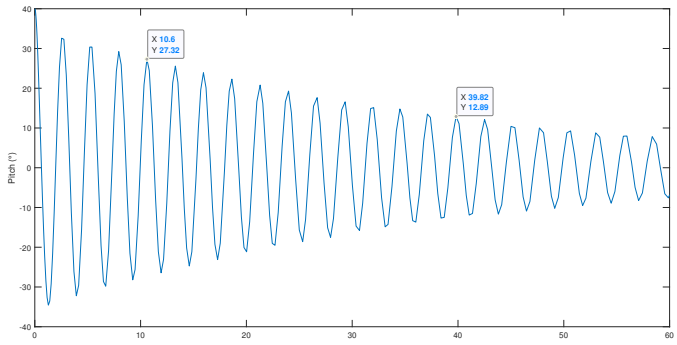

Figure 6.2: Pitch decay test with initial position=40°

From these results could be determined the natural heave and pitch periods of the cylinder. Corresponding frequencies are the following:

$$f_{nH} = 0.346Hz \text{ natural heave frequency}$$
$$f_{nP} = 0.375Hz \text{ natural pitch frequency}$$

6.2 Highlighting Parametric Resonance

6.2.1 Method

As discussed in Sect. 2.2.2, parametric resonance phenomena are most triggered when the frequency of parametric modulation (here, the incoming waves) is twice the natural frequency of the system.
The following subsections present and discuss results of simulations with varying wave inputs.

6.2.2 Body response at $f = (1/2)f_{nP}$

For wave frequencies equal to half the natural pitch frequency of the body (hence far from the optimal conditions of apparition of parametric resonance), results of simulations show a relative stability in the case of small wave amplitude. Fig.6.3 shows that for a wave amplitude of 0,2m, pitch oscillations can reach up to 7°, with a period of oscillation of 5,3s.

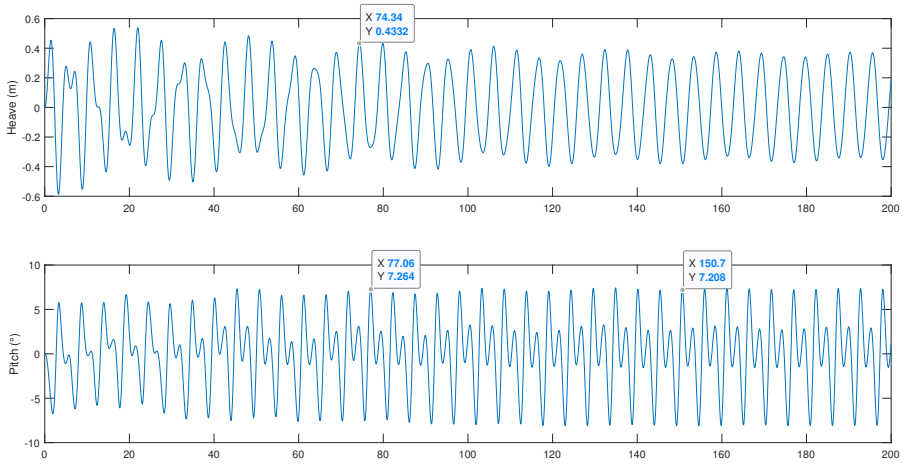

Figure 6.3: Body response for $f = (1/2)f_{nP}$ and wave amplitude=0.2m

A “double pitch oscillation” of the body can be noted and is highlighted in Fig.6.4. The body, after pitching up to its maximal angular value, returns to its initial position and is slightly tilted in the same direction as previously, before pitching in the opposite direction.

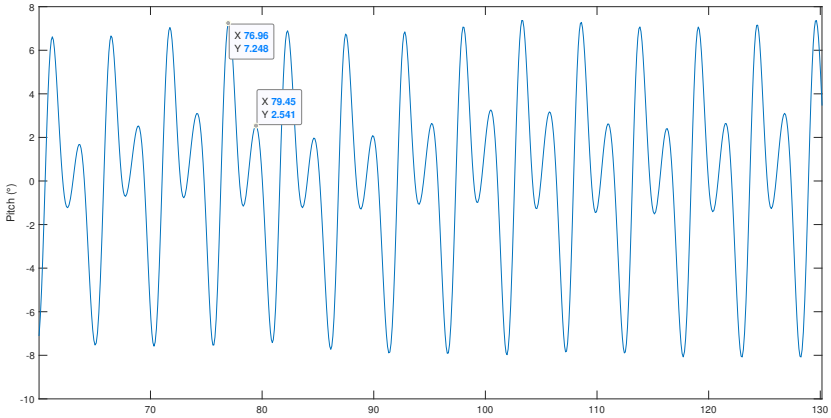

Figure 6.4: Double oscillation in the pitch response for wave amplitude=0.2m

Increasing the wave amplitude from 0.2m to 0.3m does not seem to change the heave motion amplitude but has a strong effect on pitch motion. Fig.6.5 shows that pitch oscillations can reach up to 40°with such wave amplitude. The motion is progressively dampened, reaching pitch oscillations of 10°after 200s.

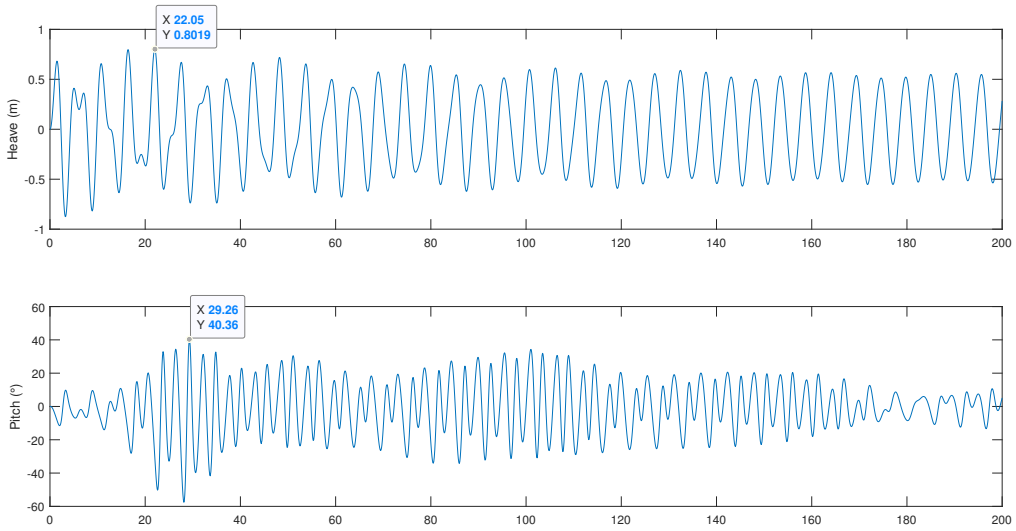

Figure 6.5: Body response for $f = (1/2)f_{nP}$ and wave amplitude=0.3m

For ever increasing wave amplitude, pitch motion quickly reaches large amplitude corresponding to the body's instability. As Fig.6.6 illustrates, increasing the wave amplitude from 0.3m to 0.4m leads to pitch motions attaining peaks up to 700°. After some time, the body gains back its "double oscillation" motion, as shown in Fig6.7.

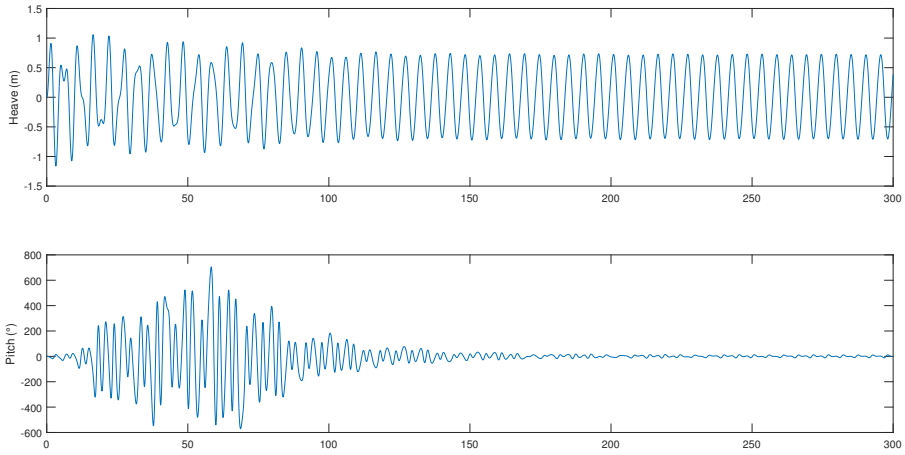

Figure 6.6: Body response for $f = (1/2)f_{nP}$ and wave amplitude=0.4m

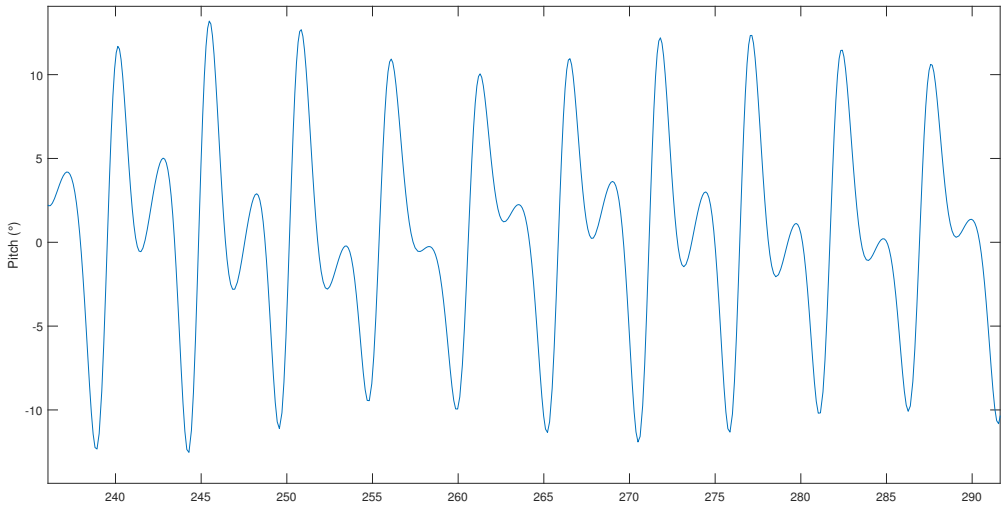

Figure 6.7: Double oscillation in the pitch response for wave amplitude=0.4m

Fig.6.8 shows the pitch motion for wave amplitude of 0,41m to 0,44m, illustrating the increasing instability of the body when the wave amplitude is slightly increased.

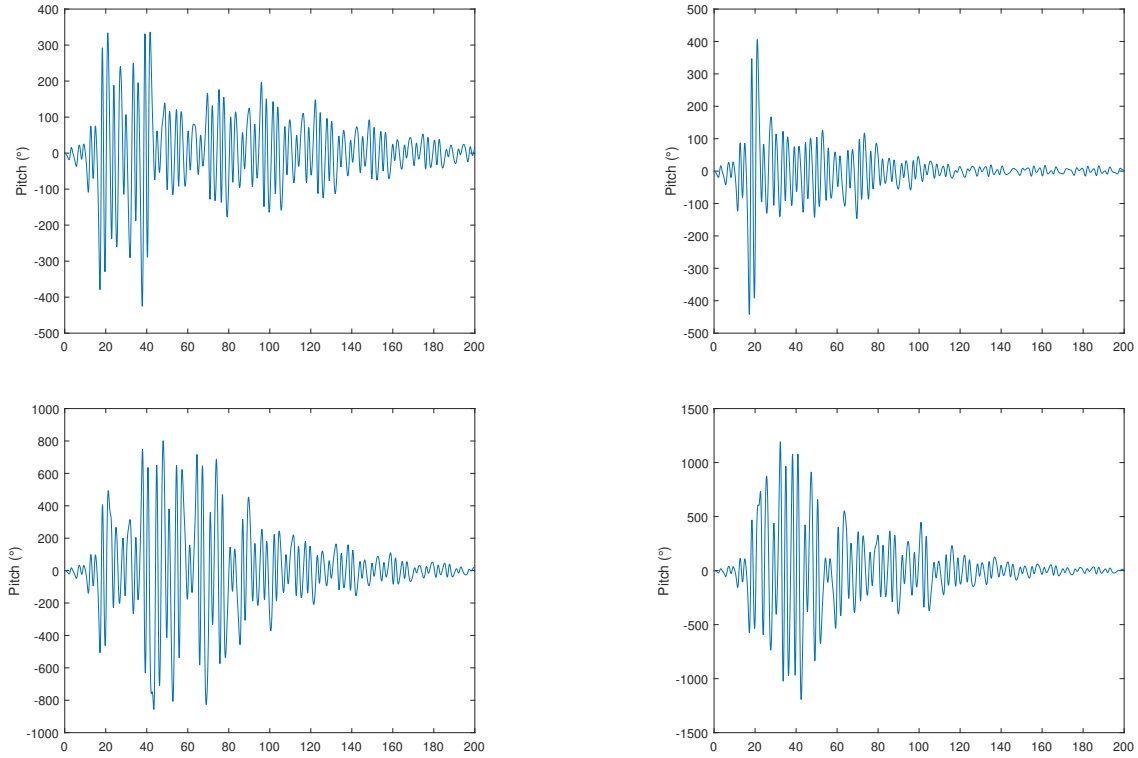

Figure 6.8: From top left to bottom right, pitch responses of the body for wave amplitudes=0.41, 0.42, 0.43, 0.44m

6.2.3 Body response at $f = 2f_{nP}$

At a wave frequency approaching twice the natural pitch frequency of the body, PR is expected to be the most triggered. Results of simulations performed at this frequency (Fig.6.9) show that parametric resonance is triggered even for relatively low wave amplitude. The body gains pitch momentum and rapidly becomes unstable, attaining pitch amplitudes up to 400°, meaning rotating on itself, with an oscillating period of 2,6s.

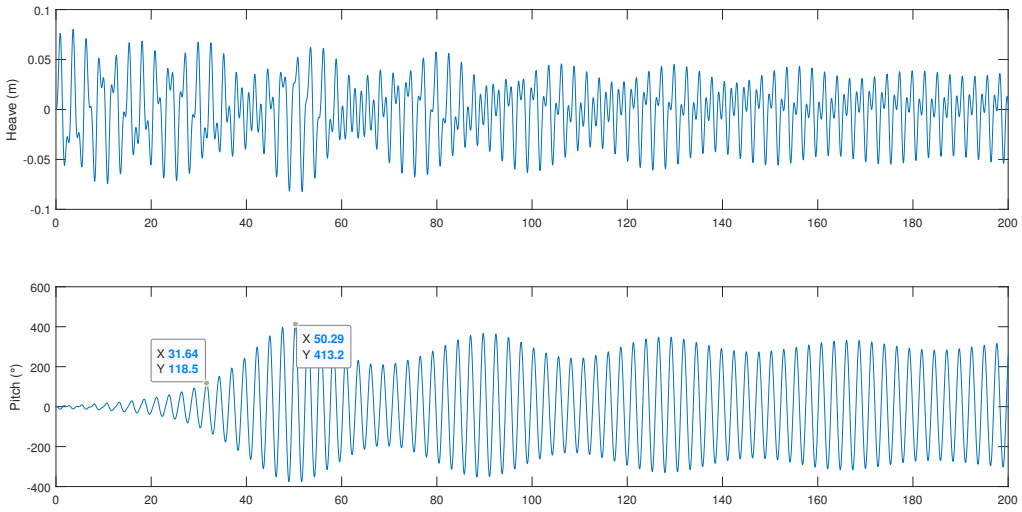

Figure 6.9: Body response for $f = 2f_{nP}$ and wave amplitude=0.1m

The results also show that heave motion is dampened when the body enters states of high pitch motion,the heave oscillations being of lower amplitude than the waves, thus that heave motion may be dampened in profit to pitch motion, as expected for real practical applications of FSBDs.

6.2.4 Body response at $f = 5f_{nP}$

Results of simulations operated for high wave frequency and amplitude show that, as for the case of low wave frequency, the response for frequencies much higher than the condition $f = (1/2)f_{nP}$ is more stable. Fig.6.10 illustrates theses results, highlighting peak pitch oscillations of 45°and a dampening of heave amplitude.
It is also highlighted in this case that when the body enters a state of stable oscillations (after 60s), its motion is operated on negative pitch values, because the incoming wave are of too high frequency to allow it to oscillate back to positive values.

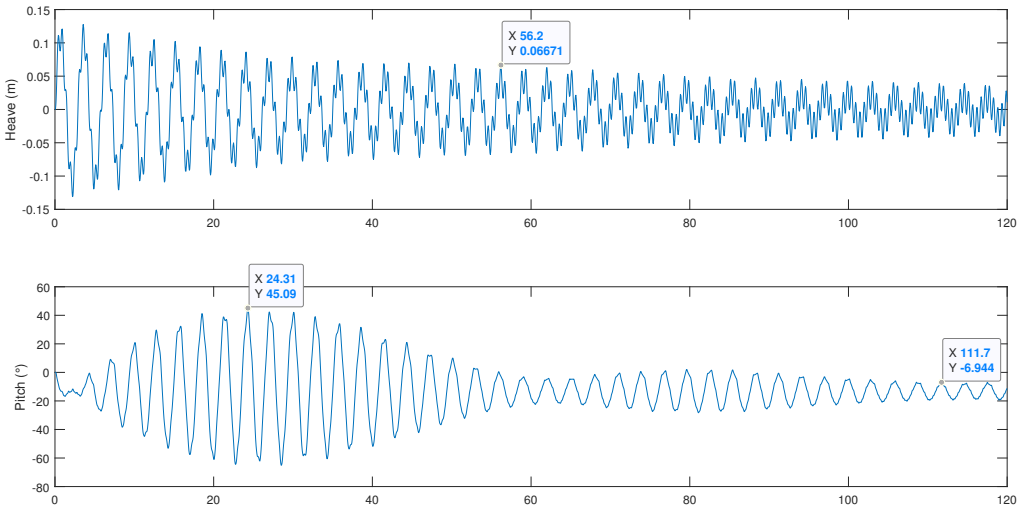

Figure 6.10: Body response for $f = 5f_{nP}$ and wave amplitude=0.6m

6.3 Discussions

These results are subject to discussion. A relative stability is observed for low wave amplitude and frequencies, and for frequencies much higher than the empirical condition of apparition of parametric resonance.
The results of simulations with wave frequency close to twice the natural pitch frequency highlight a strong instability in the pitch motion of the modelled buoy, correlating with the apparition of parametric resonance, but of effect much higher than the ones expected.
The stability of heave motion in all cases may be explained in two ways, either:

- Heave motion is converted into pitch motion by strong and unstable coupling
- The heave damping is efficient while a modelling problem occurred in the pitch damping

A treshold condition in the wave amplitude could not be highlighted for frequencies $f = 2f_{nP}$. It seems that the body gains momentum "on its own", due to a probable issue in the inertia parameters.

7 Conclusion

This work aimed not only to obtain the results for hydrodynamic simulations on a given body, but also to give an insight on the floating buoy devices principle, their applications as sensor buoys or wave energy harvesters, and the parametric resonance phenomena acting on them and on many offshore structures. I hope it can be of help for a student discovering this field of research.
Analytical as well as numerical models were looked upon, the first aiming to provide clearance on the forces in action on a submerged body. The latter were conducted to obtain tangible results, aiming to highlight the problems of pitch instability of such bodies.

Future work

Any student thinking of continuing this work could improve the model by dealing with the damping and inertia issues that seemed to arise in the results. Methods to counteract parametric resonance in floating bodies were not studied here but exist in Literature. The geometry of the model, chosen simple in this study, could be modified to create more stability, since the axiMeshRotate code can theoretically generate a mesh for any axisymmetric device. Finally, if more stable results are obtained, comparisons with existing models, linear and nonlinear, could be of great interest.

I thank the reader to taking the time and consideration to go through this document and hope that it was a clear and pleasant enough reading.

8 Appendix: MatLab code Model_run.m

```
%----------------------------------------
%Select Cylinder radius, draught and CoM
Radius=0.35;
Draught=2;
CoM=Draught-0.75;
%----------------------------------------
%%% Constants %%%
%----------------
% Density
rho = 999;      %[kg/m^3]
% Gravity
g=9.81;          %[m/s^2]
%----------------------------------------
%Moment of Inertia
m = pi*Radius^2*Draught*rho;       %Mass[kg]
I55=m/12*(3*Radius^2+(0.75*2)^2); %Inertia[kg.m^2]
%----------------------------------------
%Time
dt = 0.005;
EndTime=600;
Time=0:dt:EndTime;
%----------------------------------------
%Initial Positions
Heave1=0;
Pitch1=0;
%----------------------------------------
%%% Wave %%%
%-----------
Amplitude = 0.8; % Wave amplitude [m]
Frequency = 5*0.38; % Wave frequency [Hz]
Period=1/Frequency;
wave_w= 2*pi*Frequency; %[rad/s]
```

```
33 wave = Amplitude*sin(wave_w*Time); % Create input wave
   signal[m]
34 Wave=[Time',wave'];  %Wave vector for Simulink
35 %-----------------------------------------
36 %%%%%%%%%%%%%%%%%%%%%%%%%%%%%%%%%%%%%%%%%%%%
37 %Range of positions
38 %----------------------------
39 DRAUGHT=-4:0.2:-0.2;
40 PITCH=-40:10:40;
41 %Initialisation
42 %-----------------------------------------
43 Fe3=zeros(length(Time),length(DRAUGHT),length(PITCH));
44 Fe5=zeros(length(Time),length(DRAUGHT),length(PITCH));
45 K3=zeros(length(DRAUGHT),length(PITCH));
46 K5=zeros(length(DRAUGHT),length(PITCH));
47 invI3=zeros(length(DRAUGHT),length(PITCH));
48 invI5=zeros(length(DRAUGHT),length(PITCH));
49 %%%%%%%%%%%%%%%%%%%%%%%%%%%%%%%%%%%%%%%%%%%%
50 %Loop through positions, load data
51 for di=1:length(DRAUGHT)
52     for Pi=1:length(PITCH)
53 Draught=DRAUGHT(di);  %Submerged draught of the cylinder at
    equilibrium [m]
54 Pitch=PITCH(Pi);
55 CoM=Draught+0.75;      %Center of Mass depth below water
   line [m]
56 Cylinder=strcat('R',num2str(Radius),'D',num2str(Draught),'
   CoMz',num2str(CoM),'P',num2str(Pitch));
57 %Load Excitation force coeffcients
58 load(strcat('Nemoh_Automate/Cylinder2_',Cylinder,'/Excite.
   mat'));  %Load excitation force co-efficients - "Fe"
59 load(strcat('Nemoh_Automate/Cylinder2_',Cylinder,'/w.mat'))
   ;  %Load corresponding frequencies - "w"
60 %Calculate excitation force
61 ind=find(w<=wave_w);        %Find the excitation force co-
   efficient for that frequency
```

```
62 Fex_HeaveCoefficient = Fe(ind(end),3);
63 Fex_PitchCoefficient = Fe(ind(end),5);
64
65 Fe3(:,di,Pi)=Amplitude*(real(Fex_HeaveCoefficient)*cos(
      wave_w*Time)+imag(Fex_HeaveCoefficient)*sin(wave_w*Time))
      ;
66 Fe5(:,di,Pi)=Amplitude*(real(Fex_PitchCoefficient)*cos(
      wave_w*Time)+imag(Fex_PitchCoefficient)*sin(wave_w*Time))
      ;
67 %-----------------------------------------
68 %%% Restoring %%%%
69 %-----------------
70 %Load restoring from Nemoh and make look up table
71 load(strcat('Nemoh_Automate/Cylinder2_',Cylinder,'/KH.mat')
      );
72
73 K3(di,Pi)=KH(3,3);
74 K5(di,Pi)=KH(5,5);
75 %-----------------------------------------
76 %%% Added mass %%%
77 %-----------------
78 load(strcat('Nemoh_Automate/Cylinder2_',Cylinder,'/IRF.mat'
      ));
79 m_infHeave = m_inf(1);
80 m_infPitch = m_inf(2);
81 %We will set up a lookup table with the inverses of mass+
      added mass
82 invI_Heave = 1/(m + m_infHeave);
83 invI_Pitch = 1/(I55 + m_infPitch);
84
85 invI3(di,Pi)=invI_Heave;
86 invI5(di,Pi)=invI_Pitch;
87     end
88 end
89
90
```

```
%----------------------------------------
%%% Creating the Lookup tables %%%
%--------------------------------
%Fe3
Fe3_Table=Simulink.LookupTable;
Fe3_Table.Table.Value=Fe3;
Fe3_Table.Breakpoints(3).Value=PITCH;
Fe3_Table.Breakpoints(2).Value=DRAUGHT+2;
Fe3_Table.Breakpoints(1).Value=Time;
Fe3_Table.StructTypeInfo.Name = 'Fe3';

%Fe5
Fe5_Table=Simulink.LookupTable;
Fe5_Table.Table.Value=Fe5;
Fe5_Table.Breakpoints(3).Value=PITCH;
Fe5_Table.Breakpoints(2).Value=DRAUGHT+2;
Fe5_Table.Breakpoints(1).Value=Time;
Fe5_Table.StructTypeInfo.Name = 'Fe5';

%K3
K3_Table=Simulink.LookupTable;
K3_Table.Table.Value=K3;
K3_Table.Breakpoints(1).Value=DRAUGHT+2;
K3_Table.Breakpoints(2).Value=PITCH;
K3_Table.StructTypeInfo.Name = 'K3';

%K5
K5_Table=Simulink.LookupTable;
K5_Table.Table.Value=K5;
K5_Table.Breakpoints(1).Value=DRAUGHT+2;
K5_Table.Breakpoints(2).Value=PITCH;
K5_Table.StructTypeInfo.Name = 'K5';

%invI3
invI3_Table=Simulink.LookupTable;
invI3_Table.Table.Value=invI3;
```

```
invI3_Table.Breakpoints(1).Value=DRAUGHT+2;
invI3_Table.Breakpoints(2).Value=PITCH;
invI3_Table.StructTypeInfo.Name = 'invI3';

%invI5
invI5_Table=Simulink.LookupTable;
invI5_Table.Table.Value=invI5;
invI5_Table.Breakpoints(1).Value=DRAUGHT+2;
invI5_Table.Breakpoints(2).Value=PITCH;
invI5_Table.StructTypeInfo.Name = 'invI5';
%-----------------------------------------
%%% Damping %%%%
%---------------
% Load the State-space parameters for the equilibrium
   position (zero heave,
% zero pitch)
load('CylinderSimulink/Heave_Rad_SS.mat');
load('CylinderSimulink/Pitch_Rad_SS.mat');
%%%%%%%%%%%%%%%%%%%%%%%%%%%%%%%%%%%%%%%%%%%%%%%%%%
%-----------------------------------------
%%% Simulate %%%
%--------------
sim('Model_Simulink')
%-----------------------------------------
%%% Post Process %%%
%-------------------
t=simout.time;
heave=simout.Data(:,1);
pitch=simout.Data(:,2);
%-----------------------------------------
%%% Plot %%%
%-----------
figure,
subplot(2,1,1), plot(tout,heave), ylabel('Heave (m)')
subplot(2,1,2), plot(tout,rad2deg(pitch)), ylabel('Pitch (
    )')
```

```
%plot(tout,heave), ylabel('Heave (m)')
%plot(tout,rad2deg(pitch)), ylabel('Pitch (  )')
```

References

[1] C. Albaladejo, P. Sánchez, A. Iborra, F. Soto, J. A. López, and R. Torres, "Wireless sensor networks for oceanographic monitoring: A systematic review," *Sensors*, vol. 10, no. 7, pp. 6948–6968, 2010.

[2] P. Durand-Estèbe, *Systèmes de récupération d'énergie pour l'alimentation de capteurs autonomes pour l'aéronautique*. PhD thesis, Toulouse, INSA, 2016.

[3] S. Barstow, G. Mørk, L. Lønseth, and J. P. Mathisen, "Worldwaves wave energy resource assessments from the deep ocean to the coast," *Journal of Energy and Power Engineering*, vol. 5, no. 8, pp. 730–742, 2011.

[4] A. T. de Almeida and P. S. Moura, "Desalination with wind and wave power," in *Solar Desalination for the 21st Century*, pp. 305–325, Springer, 2007.

[5] A. Poullikkas, "Technology prospects of wave power systems," *Electronic Journal of Energy & Environment*, vol. 2, no. 1, pp. 47–69, 2014.

[6] L. F. Miles, "A permanent-magnet linear generator wave energy converter for low power ocean sensors," 2017.

[7] J. Aubry, H. B. Ahmed, and B. Multon, "Sizing optimization methodology of a surface permanent magnet machine-converter system over a torque-speed operating profile: Application to a wave energy converter," *IEEE Transactions on Industrial Electronics*, vol. 59, no. 5, pp. 2116–2125, 2012.

[8] J. Davidson, *Enery Harvesting for Marine Based Sensors*. PhD thesis, James Cook University, 2016.

[9] K. R. Tarrant, *Numerical modelling of parametric resonance of a heaving point absorber wave energy converter*. PhD thesis, Trinity College Dublin, 2015.

[10] M. Brennan, I. Kovacic, A. Carrella, and T. Waters, "On the jump-up and jump-down frequencies of the duffing oscillator," *Journal of Sound and Vibration*, vol. 318, no. 4-5, pp. 1250–1261, 2008.

[11] K. J. Åström, "Theory and applications of adaptive controla survey," *Automatica*, vol. 19, no. 5, pp. 471–486, 1983.

[12] B. Multon, A. H. Clément, M. Ruellan, J. Seigneurbieux, and H. BEN AHMED, "Systèmes de conversion des ressources énergétiques marines," in *Les Nouvelles Technologies de l'Energie*, pp. pp.221–266, Hermès Publishing, 2006.

[13] M. RUELLAN, B. ROZEL, H. Benahmed, B. Multon, A. Babarit, and A. CLEMENT, "Pre-design of direct electrical PTO for the SEAREV wave energy device," in *Coordinated Action Ocean Energy - 2nd Workshop*, (Uppsala, Sweden), 2005.

[14] H. Rao, X. Liang, Z. Xu, and J. An, "Analysis of the retransmission mechanism based on mass storage and tdm for buoy high-rate communication," in *Journal of Physics: Conference Series*, vol. 1069, p. 012132, IOP Publishing, 2018.

[15] A. H. Nayfeh and D. T. Mook, *Nonlinear oscillations*. John Wiley & Sons, 2008.

[16] S.-J. Liao, *The proposed homotopy analysis technique for the solution of nonlinear problems*. PhD thesis, Ph. D. Thesis, Shanghai Jiao Tong University Shanghai, 1992.

[17] S. Liao, *Homotopy analysis method in nonlinear differential equations*. Springer, 2012.

[18] S. Nourazar and A. Mirzabeigy, "Approximate solution for nonlinear duffing oscillator with damping effect using the modified differential transform method," *Scientia Iranica*, vol. 20, no. 2, pp. 364–368, 2013.

[19] P. Maffezzoni, L. Codecasa, and D. D'Amore, "Time-domain simulation of nonlinear circuits through implicit runge–kutta methods," *IEEE Transactions on Circuits and Systems I: Regular Papers*, vol. 54, no. 2, pp. 391–400, 2007.

[20] B. Anicin, D. Davidovic, and V. Babovic, "On the linear theory of the elastic pendulum," *European Journal of Physics*, vol. 14, no. 3, p. 132, 1993.

[21] D. J. Limebeer, R. S. Sharp, and S. Evangelou, "Motorcycle steering oscillations due to road profiling," *J. Appl. Mech.*, vol. 69, no. 6, pp. 724–739, 2002.

[22] W. Froude, "On the rolling of ships.," *Trans INA*, vol. 2, pp. 180–227, 1861.

[23] W. Froude, "Remarks on mr. scott russells paper on rolling," *Transactions of the Institute of Naval Research*, vol. 4, pp. 232–275, 1863.

[24] J. Kerwin, "Notes on rolling in longitudinal waves," *International Shipbuilding Progress*, vol. 2, no. 16, pp. 597–614, 1955.

[25] J. R. Paulling, "On unstable ship motions resulting from nonlinear coupling," *J. Ship Res.*, vol. 3, pp. 36–46, 1959.

[26] W. Kinney, "On the unstable rolling motions of ships resulting from nonlinear coupling with pitch including the effect of damping in roll," tech. rep., CALIFORNIA UNIV BERKELEY INST OF ENGINEERING RESEARCH, 1961.

[27] W. N. France, M. Levadou, T. W. Treakle, J. R. Paulling, R. K. Michel, and C. Moore, "An investigation of head-sea parametric rolling and its influence on container lashing systems," *Marine Technology*, vol. 40, no. 1, pp. 1–19, 2003.

[28] A. Olvera, E. Prado, and S. Czitrom, "Parametric resonance in an oscillating water column," *Journal of Engineering Mathematics*, vol. 57, no. 1, pp. 1–21, 2007.

[29] K. Tarrant and C. Meskell, "Investigation on parametrically excited motions of point absorbers in regular waves," *Ocean Engineering*, vol. 111, pp. 67–81, 2016.

[30] G. Giorgi and J. V. Ringwood, "Articulating parametric resonance for an owc spar buoy in regular and irregular waves," *Journal of Ocean Engineering and Marine Energy*, vol. 4, no. 4, pp. 311–322, 2018.

[31] J. Davidson, T. Kalmar-Nagy, G. Giorgi, and J. V. Ringwood, "nonlinear rock and roll–modelling and control of parametric resonances in wave energy devices," in *Proc. 9th Vienna Int. Conf. Math. Modelling*, 2018.

[32] A. Allievi and A. Soudack, "Ship stability via the mathieu equation," *International Journal of Control*, vol. 51, no. 1, pp. 139–167, 1990.

[33] V. L. Belenky, K. M. Weems, W.-M. Lin, and J. R. Paulling, "Probabilistic analysis of roll parametric resonance in head seas," in *Contemporary Ideas on Ship Stability and Capsizing in Waves*, pp. 555–569, Springer, 2011.

[34] B. van der Pol and M. Strutt, "Ii. on the stability of the solutions of mathieu's equation," *The London, Edinburgh, and Dublin Philosophical Magazine and Journal of Science*, vol. 5, no. 27, pp. 18–38, 1928.

[35] G. Giorgi and J. V. Ringwood, "Computationally efficient nonlinear froude–krylov force calculations for heaving axisymmetric wave energy point absorbers," *Journal of Ocean Engineering and Marine Energy*, vol. 3, no. 1, pp. 21–33, 2017.

[36] A. Clement and P. Ferrant, "Superharmonic waves generated by the large amplitude heaving motion of a submerged body," in *Nonlinear Water Waves*, pp. 423–433, Springer, 1988.

[37] J. Falnes, *Ocean waves and oscillating systems: linear interactions including wave-energy extraction*. Cambridge university press, 2002.

[38] A. Merigaud, J.-C. Gilloteaux, and J. V. Ringwood, "A nonlinear extension for linear boundary element methods in wave energy device modelling," in *ASME 2012 31st International Conference on Ocean, Offshore and Arctic Engineering*, pp. 615–621, American Society of Mechanical Engineers, 2012.

[39] M. Penalba Retes, A. Mérigaud, J.-C. Gilloteaux, and J. Ringwood, "Nonlinear froude-krylov force modelling for two heaving wave energy point absorbers," in *Proceedings of the 11th European Wave and Tidal Energy Conference*, European Wave and Tidal Energy Conference 2015, 2015.

[40] W. Cummins, "The impulse response function and ship motions," tech. rep., David Taylor Model Basin Washington DC, 1962.

[41] T. Bjarte-Larsson and J. Falnes, "Laboratory experiment on heaving body with hydraulic power take-off and latching control," *Ocean Engineering*, vol. 33, no. 7, pp. 847–877, 2006.

[42] M. A. Bhinder, M. Rahmati, C. G. Mingham, and G. A. Aggidis, "Numerical hydrodynamic modelling of a pitching wave energy converter," *European Journal of Computational Mechanics*, vol. 24, no. 4, pp. 129–143, 2015.

[43] G. De Backer, M. Vantorre, K. De Beule, C. Beels, and J. De Rouck, "Experimental investigation of the validity of linear theory to assess the behaviour of a heaving point absorber at the belgian continental shelf," in *ASME 2009 28th International Conference on Ocean, Offshore and Arctic Engineering*, pp. 1013–1020, American Society of Mechanical Engineers Digital Collection, 2009.

[44] C. Brebbia and J. Dominguez, "Boundary element methods for potential problems," *Applied Mathematical Modelling*, vol. 1, no. 7, pp. 372–378, 1977.

[45] G. K. Politis, "Application of a bem time stepping algorithm in understanding complex unsteady propulsion hydrodynamic phenomena," *Ocean Engineering*, vol. 38, no. 4, pp. 699–711, 2011.

[46] G. Rus, S.-Y. Lee, and R. Gallego, "Defect identification in laminated composite structures by bem from incomplete static data," *International journal of solids and structures*, vol. 42, no. 5-6, pp. 1743–1758, 2005.

[47] M. Penalba, T. Kelly, and J. V. Ringwood, "Using nemoh for modelling wave energy converters: A comparative study with wamit," in *Proceedings of the 12th European Wave and Tidal Energy Conference (EWTEC2017), Cork, Ireland*, vol. 27, pp. 631–1, 2017.

[48] J. S. Shamma and M. Athans, "Analysis of gain scheduled control for nonlinear plants," *IEEE Transactions on Automatic Control*, vol. 35, no. 8, pp. 898–907, 1990.

[49] D. J. Leith and W. Leithead, "Gain-scheduled and nonlinear systems: dynamic analysis by velocity-based linearization families," *International Journal of Control*, vol. 70, no. 2, pp. 289–317, 1998.

[50] A. McCabe, G. A. Aggidis, and T. Stallard, "A time-varying parameter model of a body oscillating in pitch," *Applied Ocean Research*, vol. 28, no. 6, pp. 359–370, 2006.

[51] N. Faedo, Y. Peña-Sanchez, and J. V. Ringwood, "Finite-order hydrodynamic model determination for wave energy applications using moment-matching," *Ocean Engineering*, vol. 163, pp. 251–263, 2018.

[52] Y. Pena-Sanchez, N. Faedo, M. Penalba, G. Giorgi, A. Mérigaud, C. Windt, D. G. Violini, L. Wang, and J. V. Ringwood, "Finite-order hydrodynamic approximation by moment-matching (foamm) toolbox for wave energy applications,"